

Characterization of injection and confinement improvement through impurity induced profile modifications on the Wendelstein 7-X stellarator

R. Lunsford^{1,a)}, C. Killer², A. Nagy¹, D. A. Gates¹, T. Klinger², A. Dinklage², G. Satheeswaran³, G. Kocsis⁴, S. A. Lazerson², F. Nespoli¹, N. A. Pablant¹, A.v. Stechow², A. Alonso⁵, T. Andreeva², M. Beurskens², C. Biedermann², S. Brezinsek³, K. J. Brunner², B. Buttenschön², D. Carralero⁵, G. Cseh⁴, P. Drewelow², F. Effenberg¹, T. Estrada⁵, O. P. Ford², O. Grulke², U. Hergenrohn^{2,b)}, U. Höfel², J. Knauer², M. Krause², M. Krychowiak², S. Kwak², A. Langenberg², U. Neuner², D. Nicolai³, A. Pavone², A. Puig Sitjes², K. Rahbarnia², J. Schilling², J. Svensson², T. Szepesi⁴, H. Thomsen², T. Wauters³, T. Windisch², V. Winters², D. Zhang², L. Zsuga⁴ and the W7-X team^{2,c)}

¹ Princeton Plasma Physics Laboratory, Princeton, NJ USA 08540

² Max-Planck-Institut für Plasmaphysik, Greifswald, Germany 17491

³ Forschungszentrum Jülich, IEK-4 Plasmaphysik, Jülich, Germany 52428

⁴ Center for Energy Research, Budapest, Hungary 1121

⁵ Fusion National Laboratory, CIEMAT, Madrid, Spain 28040

a) E-mail : rlunsfor@pppl.gov

b) Currently at: Fritz-Haber-Institut der Max-Planck-Gesellschaft, Faradayweg 4-6, 14195 Berlin, Germany.

c) For the Wendelstein 7-X Team, see the author list: T. Klinger et al., 2019 *Nucl. Fusion* **59**, 112004 doi.org/10.1088/1741-4326/ab03a7

Pulsed injections of boron carbide granules into Wendelstein 7-X stellarator (W7-X) plasmas transiently increase the plasma stored energy and core ion temperatures above the reference W7-X experimental programs by up to 30%. In a series of 4MW ECRH heated experiments, the PPPL Probe Mounted Powder Injector provided 50 ms bursts of 100 micron granules every 350 ms at estimated quantities ranging from approximately 1 mg/pulse to over 30 mg/pulse. For each injection the stored energy was observed to initially drop and the radiated power transiently increase, while the radial electron density profile rose at the edge as material was assimilated. Once the injected boron carbide was fully absorbed, the density rise transitioned to the core while the stored energy increased above the previous baseline level by an amount linearly correlated with the injection quantity. During the injections, the ion temperature gradient steepened with peak core ion temperatures observed to increase from a nominal 1.7 keV to over

2.6 keV for the largest injection amounts.. Enhanced performance is accompanied by a reversal of the radial electric field at $\rho < 0.3$, indicating the core transport has switched to the ion root. These observations are suggestive of a change in transport and provide further evidence that externally induced profile modifications provide a possible path to enhanced W7-X performance metrics.

1. Introduction

As fusion research transitions to long pulse devices with the goal of achieving steady state operation, both the methods of providing excellent first wall conditions as well as maintaining their status throughout the duration of the discharge will need to be augmented. For example, a consequence of “always on” superconducting magnets, such as those on W7-X[1], EAST[2], KSTAR[3], LHD[4], and WEST[5] is that premium wall conditions cannot be restored by between discharge volume breakdowns. This commonly employed method, termed “glow discharge cleaning”(GDC)[6], is prevented by the shaped magnetic fields[7]. By the same token, depositional volume breakdown coating methods such as boronization[8] cannot be employed while the magnetic field is energized and thus require a cessation of operations[9]. Given a desire to extend magnetic coil lifetime by minimizing current cycling events, it would be programmatically advantageous to develop alternate methods to modify wall conditions or getter rising hydrogen levels within standard operational conditions.

The injection of milligram quantities of low-Z particulate impurities through the use of an Impurity Powder Dropper (IPD)[10] has resulted in discharge improvements in a number of the world’s leading fusion research devices. The introduction of lithium and/or boron powder into NSTX[11], EAST[12, 13] and KSTAR[14] has led to the mitigation or elimination of ELMs, while boron pulses have led to an increase in confined electron and ion temperatures in LHD[15]. Improvements to overall discharge performance have also been observed on AUG in response to the injection of boron nitride[16]. In addition, the application of particulate based conditioning methods has been shown to beneficially alter the plasma material interface on DIII-D[17], NSTX-U[18], EAST[19], ASDEX[20] and most recently on LHD. In these instances, the gravitational introduction of aerosolized powders, either Li, B, or BN has been observed to have lasting (inter-discharge) effects similar to traditional wall conditioning methods[21-23]

Given programmatic constraints, a full powder dropper installation on the Wendelstein 7-X stellarator (W7-X) was deemed temporarily impractical, and as such an alternate technology was required. A vacuum compatible periodic particle source termed the Probe Mounted Particle Injector(PMPI)[24] was developed

and installed on the W7-X Multi-Purpose Manipulator (MPM)[25] probe allowing direct injection of impurities. The initial objectives of the PMPI experiments were to assess the ability of a single injector to effectively distribute conditioning material within a stellarator geometry and if possible, to determine if a particulate injection system had a beneficial effect upon W7-X wall conditions. While results of the experiments vis-a-vis improved conditioning were inconclusive, important information was observed about impurity entrainment and distribution throughout the vessel. In addition, these periodic pulsed injections were also observed to generate an unexpected transient performance boost.

In this paper we outline the operational envelope of the PMPI and describe the first experiments undertaken with this new actuator. This includes observations of full toroidal transport of the injected material as well as a discussion of the supplemental calibration utilized to better characterize the quantity of injected material. After this we classify plasma responses to the impurity injections and conclude with a discussion detailing how those plasma modifications lead to the observed beneficial effects on overall plasma performance.

2. Experimental Apparatus

Due to program requirements for mainline diagnostic commissioning prior to the most recent Operational Period of W7-X (OP1.2) it was determined that it would not be practical to install a fully integrated Impurity Powder Dropper(IPD) as was done on other devices. The arrived upon solution was to create a modified powder injector which would allow initial experiments to be performed utilizing a temporary installation on the W7-X Multi-Purpose Manipulator[25] probe arm. The primary impetus behind the design and implementation of the PMPI was to facilitate rapid deployment of a particulate impurity source thus allowing a characterization of the behavior of injected impurities within the W7-X topology prior to the extended programmatic upgrade between the preliminary commissioning phase of W7-X (OP1) and the latter initial research phase (OP2). The focus of these initial injection experiments was to determine the ability of a single source impurity actuator to transport injected material throughout the vessel while assessing the stability of the discharge to the repeated introduction of solid material. These results would then provide insight into the ability of a full IPD system to operate effectively within the constraints of a stellarator operational space.

2.1. The PPPL Probe Mounted Particle Injector (PMPI)

This is the author's peer reviewed, accepted manuscript. However, the online version of record will be different from this version once it has been copyedited and typeset.

PLEASE CITE THIS ARTICLE AS DOI: 10.1063/5.0047274

The PPPL PMPI was custom designed to provide a portion of the functionality of the PPPL Impurity Powder Dropper (IPD) system deployed on AUG[20], EAST[19] and DIII-D[17] within the cylindrical operational envelope of the MPM (120mm diameter x 150mm length). To accomplish this the PMPI is designed with a single impurity hopper/feeder pair as shown in figure 1 as opposed to the 4 feeders found in the standard IPD. A cylindrical column and funnel, comprising an 80 cm³ volume maintains the powder inventory. The feeder tray, located 2mm below the bottom of the funnel, is vibrated at resonance and this movement conveys powder down the tray towards the impeller wheel. As the major change between the operational methodology of the IPD and PMPI is the need to provide for horizontal rather than gravitational injection a piezoelectric rotary motor specifically designed for operation in high field environments was coupled to a vertically oriented paddle wheel. The eight 35mm long vacuum compatible thermoplastic polyether-ether-keytone (PEEK) blades attached to the central hub are machined to be slightly longer than the distance from the wheel hub to the bottom of the feed tray. During rotation the paddles flex slightly when coming in contact with the aluminum tray scraping powder along the tray and bringing it forward. As each paddle passes the vertical axis the flexure energy is released providing the majority of the 0.5 m/s injection velocity. The powder is projected up and forward out of the feeder tray as shown in panel a) of figure 2. The quantity of powder delivered is determined by the depth of powder in the tray and can be roughly controlled by altering the excitation amplitude of the sinusoidal signal sent to the piezoelectric crystals connected to the feeder tray. At normal operation, this provides a pulsed injection every 350 ms. Laboratory tests in atmosphere have shown a maximum horizontal throw of 25 cm with the majority of the powder delivered within the range of 12 to 18 cm[24]. The need for a compact mechanical method of horizontal introduction was the primary driving force behind the actuator design and is responsible for the pulsed nature of injections from the PMPI as opposed to the more continuous flow observed during IPD operations. The entirety of the PMPI assembly is enclosed within a protective graphite covering into which a 13 mm x 20 mm rectangular hole has been machined on the front to allow for powder injection. For these experiments the PMPI was filled with 80 mL of loose packed granular boron carbide powder for a total inventory of approximately 100 grams.

To deliver the boron carbide payload to the discharge, the PMPI is mounted to the head of the W7-X Multi-Purpose Manipulator and relayed past the vacuum boundary into the main chamber. The MPM is designed as a unique multi-user platform for plasma edge investigations and facilitates a variety of measurements through rapid replacement of diagnostic heads without the need to disrupt the W7-X main chamber vacuum conditions. For these experiments the MPM moves the PMPI probe head past the gate

valves and cryostat to a parking position in line with the outer main chamber walls. During experiments the probe was moved to locations up to 15 cm past the inner wall, a position which, based on measured SOL profiles[26], left it external to the discharge by amounts ranging from 20 cm at the furthest to 5 cm at the closest. These standoff distances allowed the probe extended dwell time at this location without substantial heat buildup on the probe's graphite shield. We note that at the shorter distances, heating of the protective carbon shell was observed during the course of the 7s plasma exposure, although measurements on the onboard thermocouple showed the PMPI temperature to still be well within operational range.

2.1.1. Choice of Incident Injection Media

The coating of interior plasma facing surfaces is an effective way to control hydrogenic recycling and reduce impurity influx. To minimize the impact of sputtered coating material on the effective ion charge of the plasma, low atomic number species are often selected as the materials of choice for injection. Examples include lithium, boron, and silicon delivered through evaporative coating, volume glow discharge depositional coating and plasma assisted coating. The standard version of the IPD has been successfully tested with Li, B, BN, B₄C, C, SiC, and Sn. During wall conditioning experiments on other devices, the standard gravitationally fed IPD is nominally loaded with a subset of lithium, pure boron powder, or boron nitride as the needs of the host scientific program dictate. Lithium was not a preferred option for these initial tests on W7-X and so the choice of injection material was narrowed to a boron containing compound.

Previous experiments have shown that the concomitant nitrogen introduced with BN behaves in a similar manner as injected nitrogen gas and sharply raises the radiative fraction of the discharge. As such, it places a more stringent limit on the amount of material that can be injected prior to the onset of a radiative discharge collapse. Pure boron powder does not lead to these sharp increases in plasma radiation, and as such would have been the preferred choice of injection material. However, it has been observed that under certain conditions the boron powder load can tend to aggregate and form clumps which inhibit material flow and thus optimal performance within a standard IPD. When the system is mounted external to the vacuum vessel, identifying and resolving this issue is a minor inconvenience, however as the PMPI is internal to the vacuum boundary, such clumping could not be easily remedied. It

was determined therefor that boron carbide would be a better choice of injection medium as the carbon within the crystalline lattice acts in a manner similar to a graphite lubricant and keeps the particulate flow clump free. The material utilized here is of the same stock as was previously analyzed in figure 4 of [27] and injected into DIII-D[28] for multi-species granule experiments and was thus deemed suitable for injection into a research plasma environment.

2.2. Wendelstein 7-X

Wendelstein 7-X is a five-fold symmetric stellarator of major radius 5.5m and minor radius 0.5m with an interior plasma volume of about 30 m³. The magnetic flux surfaces are generated by a set of external planar and non-planar superconducting coils and the field geometry has been drift optimized to minimize neoclassical transport losses while maintaining MHD stability[29, 30]. Primary plasma heating through electron cyclotron resonance heating(ECRH) supports moderate densities (relevant to this paper $< 0.5 \times 10^{20} \text{ m}^{-3}$) with electron temperatures $T_e \sim 5 \text{ keV}$ and ion temperature $T_i < 1.6 \text{ keV}$ in quasi-stationary discharges. In anticipation of stable high-beta operation, consistent control of first order heat loading at 10 island divertor modules has been achieved[31-33] and power and particle exhaust during the two most recent operational phases, OP1.2a and OP1.2b, are controlled through the use of this helically shaped island divertor concept[34-36].

To provide suitable machine conditions the inner plasma facing components (PFC) were covered with graphite tiles while baking as well as glow discharge cleaning (GDC)[37] provided a baseline set of conditions for the experimental campaign. To maintain wall conditions a series of short ECRH pulse trains, immediately followed by pumping intervals was employed to reduce the PFC outgassing rate[38]. In addition, experiments were alternately run with hydrogen and helium working gasses to desorb first wall hydrogen content providing enhanced density control[21, 22]. After three out of the thirteen experimental weeks of OP1.2b, a deposited boron coating was applied through a volume breakdown helium glow discharge doped with a 10% concentration of diborane gas (B_2H_6). The 4 hour boronization discharge deposited an approximately 100nm boron coating on the plasma facing components and was observed to reduce the normalized influx of oxygen and carbon by factors of approximately 10 and 4 respectively indicating gettering by the boron layer[23]. These boronization conditioning discharges were run three times over the course of the experimental campaign.

2.2.1. W7-X Diagnostics

Diagnostics on the W7-X stellarator provide well resolved measurement of plasma characteristics. Electron temperature and density profiles are provided by Thomson scattering[39, 40] while the line averaged density is measured by a dispersion interferometer[41] and measurements of the plasma stored energy are derived from a compensated set of three diamagnetic loops[42]. Impurity levels within the discharge are measured by the High-Efficiency XUV Overview Spectrometer(HEXOS)[43] and divertor imaging is provided by a visible camera equipped with a Carbon III spectroscopic line filter[44].

The overview visible camera array[45] provides images through ten ports with tangential plasma views. Camera heads at the end of a series of bellows generate observational viewing cones which stretch through the module where the respective ports are located and terminate in a line of sight intersection with the vacuum vessel in the adjacent module as can be seen in figure 3. These camera views are labelled with the moniker AEQ##, with the first number denoting the module where the port is located and the second number, either '0' or '1', denoting if the view is clockwise or counter-clockwise around the vessel respectively. For example, mounted onto the AEQ31 port (purple box in figure) is the counter-clockwise viewing camera in module 3 which directly observes the PMPI injection located in the middle of module 4. For the odd numbered ports, the camera views the interior of the module where it is located as well as the adjacent increasing number module (i.e. AEQ11 view terminates in module 2 and the AEQ51 view terminates in module 1 as the circuit is completed). Even numbered observational ports record views clockwise from the camera origin into the decreasing module number(i.e. the AEQ50 view terminates in module 4). The need for this precise distinction comes from utilizing these images and specifically their time history to track illuminated structures as they transit the vessel as will be discussed in section 3.1.

Ion temperature measurements as well as measurements of the radial electric field are determined by monitoring the perpendicular velocity of non-perturbing seeded argon gas utilizing the X-ray Imaging Crystal Spectrometer (XICS)[46, 47]. Measurements of the highly ionized Ar dopant (Ar^{16+} , Ar^{17+}) provides flow velocities from a doppler shifting of the emission lines as well as ion temperature through analysis of the line broadened spectroscopic signal. The radial electric field can then be inferred from the radial component of the local force balance equation using the flux surface averaged perpendicular flow velocity[48].

Finally, the Doppler Reflectometer(DR) system[49-53], located at the AEA21 port, injects microwave radiation at a scanned frequency from 50 to 75 GHz in steps of 1 GHz every 10 ms to monitor spatio-temporal evolution of density fluctuations. Utilizing transmitted and received signals, the distance to a reflecting layer within the plasmas is recorded. A fixed probe beam angle of $\alpha = 18^\circ$ is sensitive to density perturbations with finite perpendicular wave number such that $k_{\perp}\rho_i \sim 1$ providing a measure of the perpendicular rotation velocity. By observing the power of the back scattered signal, radially resolved density fluctuations can also be obtained. This current experimental layout of this system is described in Ref [54]. Of note, an attenuation of the fluctuation level during periods of enhanced confinement, such as after a series of fuel pellet injections[55] has been observed to indicate a change in the nature or intensity of the turbulence structures.

3. Experiment

For these experiments, repeated pulses of 100 micron diameter B₄C granules were injected into a series of W7X discharges at varying quantities to evaluate plasma robustness to injection, gross toroidal impurity transport, and any effects on plasma performance. Over a series of 7 discharges injection quantity was varied from approximately 1 mg/pulse to 30 mg/pulse and the location of the front face of the PMPI was varied between 20 and 5 cm from the nearest island scrape off layer. The closest point of approach placing the front of the PMPI approximately 10 cm from the last closed flux surface(LCFS). Injection frequency was maintained at 2.8 Hz throughout the experimental series as this represented the maximum angular velocity of the rotational motor and ensured the longest horizontal throw. For this injection frequency the laboratory measured injection velocity was 0.5 m/s. Based on the duration of ablation and estimated injection velocity we anticipated a radially injected granule to penetrate roughly 5cm into the discharge as shown in panel c) of figure 2. We note however that this injection velocity figure is only valid prior to the beginning of ablation at which point the granules become charged and respond to the electromagnetic forces present. Most specifically, the rapid influx of fast electrons responsible for ablation result in granules within the cloud becoming negatively charged and electrostatically repelling each other leading to accelerated cloud dispersal as observed in the overview camera images.

3.1. Gross Toroidal Impurity Transport

First order observations of toroidal impurity transport are provided by an array of high speed (100Hz) survey cameras installed on W7-X. The array of images in figure 4 shows the evolution of illuminated field aligned structures resulting from an injection event. The field of view of the AEQ20 camera used here is toroidally opposite of the PMPI location. The injection occurs at 5.07s and the first image in the series shows the camera view before material has transited the vessel. As can be seen in the next panel, the injected material results in a series of distinct illumination bands with the peak of the injection as seen in the third panel exhibiting extended edge radiation bands. A comparison of the first and last images shows that the dissipation of the distinct edge illuminated structures occurs more quickly than the decay of overall discharge radiation. Given the visible spectral response of these cameras, the higher ionization states of the boron in the core would not be recorded by these images and as such this widespread illumination is indicative of strong poloidal mixing of the injected boron within the discharge edge.

Similar responses can be observed in all 5 modules in response to injection. The concurrent images from multiple camera locations at $t = 5.12\text{s}$ can be seen in the photo array displayed in figure 5. The large center panel displays the image recorded by the camera installed at the AEQ31 port which is focused on the MPM location, and thus the PMPI injections. The injection pulse highlighted here started 50 ms prior to the images shown. Between the pulse initiation and the time of the frames displayed in these images the material has transited throughout the vessel. A frame by frame integration of the pixel intensities within the camera images generates a time history of the injection event and by then correlating signal intensity rises with the camera image plane location a rough estimation material spread can be determined. In figure 6, the first indications of the injected pulse come from the AEQ31 view, corresponding to a direct observation of the MPM location. Increased signal coincident with the arrival of radiative impurities is next observed by cameras associated with the AEQ40 and AEQ50 ports which have views directly clockwise and counterclockwise to the PMPI location respectively. The simultaneous observation by both cameras and the further rise in all other cameras indicates that there is not a dominant preferential streaming direction for the recently entrained impurities. Fitting curves to the intensities and examining the gap between peak illumination times in the AEQ31 and AEQ51 camera views provides a time of flight for the pulse of approximately 15 ms which gives an approximate toroidal entrainment velocity of 1200 m/s with an estimated error of ± 400 m/s.

The in-situ particle deposition method of wall conditioning is envisioned as supplemental to a standard boronization. With an initial conditioning volume breakdown being utilized to coat all interior surfaces of

the vacuum vessel, the introduction of boron particulates into nominal W7-X discharges would provide a deposition of injected material onto high fluence plasma surfaces such as limiters and divertors to extend the coating lifetime and to maintain overall peak performance. Observations of the interaction between the injected material and these components was undertaken to ensure that there is strong engagement between the injected material and some of the surfaces where conditioning is required. The upper panels of figure 7 display Carbon III filtered images of the Module 1 upper divertor during an injection series. These images show a substantially enhanced carbon signal during the injection period. Given that the boron and carbon are injected concurrently, it is reasonable to assume that there is a substantial presence of boron also engaging with the divertor surface. With experiment 20180927-47 undertaken in the 5/5 standard configuration a field line trace from the estimated injection location is shown in the lower panel of figure 7. The PMPI and the start of the material evolution is outlined in the box labelled a) where the red line is a single field line starting at $R = 6.04\text{m}$. This location represents the approximate penetration depth for a nominally injected granule as estimated by the injection velocity and ablation duration. The field line is then evolved for $\sim 100\text{m}$, illustrating a field-parallel pathway throughout the vacuum vessel. We note that this trace includes the module one upper divertor, also shown in figure 7 within a dashed box labelled b).

The trace provides an indication where direct deposition of material may occur, however we note that these initial field line tracings do not account for any dispersion within the discharge or poloidal spread in the injected material. As can be seen by the presence of the bright bands in the top middle panel of figure 7, there is a substantial volume circulation of injected material which can be understood by noting that the material introduction provided by the PMPI, as seen in the large central panel of figure 5, is not point-like and as such we can anticipate a substantial evolution of material throughout the vessel.

3.2. Quantification of injection quantities

Due to the stochastic nature of the coupling between the PEEK paddles and the material within the feeder tray, as well as variances in powder depth occurring during conveyance from the reservoir to the paddles, there is substantial discrepancy in the quantity of material disbursed by each PMPI pulse. While the injector was never intended to deliver precision quantities of material it is nevertheless possible and appropriate to attempt to determine an approximate injection quantity per pulse for initial analysis purposes.

A calibration of the feeder flow rate was performed prior to installation on W7-X and can be found in Ref[24]. It was also determined that the average coupling efficiency between the PEEK paddle and the material contained within the tray is approximately 50%. That is, 50% of the material within the tray is projected upward and forward into the plasma while the remaining material is captured by the lip on the carbon cap just in front of the feeder tray. This feature was designed to direct insufficiently accelerated particulates to an open area in the bottom of the protective carbon cap just underneath the PMPI structure. As an example mass throughput calculation we note that during the experimental program W7X20180927-07 the average throughput of the feeder tray at the voltage selected for this discharge was 6 mg/s based upon laboratory calibration. Given a paddle frequency of 2.8 Hz in conjunction with the 50% injection efficiency, this provides an estimated material injection quantity of approximately 1mg/pulse.

These pulses are then further characterized by correlating the laboratory calibration with images of the injection events as provided by the overview video diagnostic system[56], a representative image of which is illustrated in figure 2b). Given the stochastic toroidal spread of the material, the only way to ensure that the majority of the PMPI injection was accounted for was to observe it directly at the injection point. With this in mind, the illumination provided by the fast visible camera was chosen to provide a post-facto quantification. Experimental program 20180927-07 was chosen as a reference injection discharge as the PMPI was programmed for a minimal excitation level and thus we believe the injections to be well characterized. The left panel of figure 8 displays the evolution of plasma parameters P_{ECRH} , P_{RAD} , n_e , T_e , T_i , and W_{DIA} showing the minimal plasma response to small injections while the right panel shows a time history of injection events. This series was generated by performing a background subtracted summation of the pixel intensities in the area around the PMPI. The video images of the injection events from this experimental program are then compared to the peaks to determine which events are due to powder injection and these are denoted in the figure by the red arrows. Peaks following injection events are integrated to determine total ablation generated illumination and the average of the first 12 pulses was utilized to determine an empirical conversion factor between signal intensity and calibrated injection amount. The final pulse, being over a factor of 2 larger than any other injection event in this discharge, and thus indicative of an off normal event, was not included in the average. Completing this process leads to an estimated conversion factor of 4.2×10^6 counts/gram with a standard deviation of 2.2×10^6 counts/gram. A nominally linear response of the CMOS sensor over the intensity range then allows us to

utilize this conversion factor to estimate injection quantities in future discharges with larger injection amounts.

This method of post-facto calibration does not come without qualifications and limitations. In general the illumination generated by impurities can be highly dependent upon material density as well as electron density and temperature. However, as the penetration depth of the granules prior to full ablation is on the order of 5cm and as the camera is only sensitive to visible emissions we assert that the images being recorded are generated at the outer edge of the discharge. Here the profile characteristics are dominated by edge interactions and recombination and as such are fairly consistent over the course of injections allowing some confidence in pulse to pulse and shot to shot comparisons. Another limitation on the accuracy of this conversion is the observation that for many injections a substantial fraction of the illuminated pixels were saturated. As such, values obtained utilizing the conversion factor should be viewed as an approximate lower bound on injection quantity. The upper bound then being provided by the quantity of material conveyed by the powder feeder portion of the PMPI, understandable as the injector cannot disburse more material than is physically present. Thus, while this method of supplemental calibration is insufficient for a strict quantitative analysis of the injection driven events reported later in this work, it does provide a framework to allow an initial classification of the results.

Given the limitations of the camera based conversion factor it is reasonable to question the value of this numeric over a simple application of the laboratory calibration. The need for supplemental calibration of the injection quantities was dictated by an observed strongly increasing level of material injection recorded during experimental program 20180927-47 as seen in the illumination history shown in the top panel of figure 9. For this discharge, the front of the PMPI was moved to major radius $r = 6.13\text{m}$ which places it 5cm from the island scrape off layer and the piezoelectric vibration was set to produce approximately 40 mg/pulse in an effort to generate maximum particle entrainment. These settings resulted in a series of increasing injection amounts over the course of the discharge. This ramping of the injection quantity can be understood if one observes that there is a delay between the programmatic request for an increased powder injection rate, as was done for this discharge, and the full delivery of that rate as caused by the transit time for the thicker layer of powder to traverse the feeder tray and reach the impeller blades. As such the injection output is only anticipated to approach the calibrated PMPI output near the end of the injection series. Applying the previously arrived at calibration factor we can estimate the range of injected material deposited into the discharge to vary from $\sim 1\text{ mg/pulse}$ to over 30 mg/pulse

with the possibility of injections reaching 60 mg/pulse. Panels (a)-(c) shown on the lower half of figure 9 display single frame camera images which illustrate the variation in optical signature observed with different quantities of powder injection. In these images the PMPI is located midway down the right hand side of the image. Here we observe a rapid integration of material into the scrape off layer of the discharge, and for the largest injection, obvious entrainment of radiative material into field aligned structures.

To further check this method, the spectroscopic boron-V signal at 4.857 nm provided by the HEXOS diagnostic was examined. The integrated injection peaks were compared to the initial pulse and a relative injection quantity was determined. Again, assuming this initial injection consistent with laboratory calibrations, and thus representative of approximately 1 mg/pulse as was found with the the camera method we find that the relative intensities of the subsequent peaks to be largely in agreement with the survey camera method. The utilization of the survey camera method was chosen as the preferential method as the injected powder was observed to transit the interior of the vessel in both a clockwise and counter-clockwise manner, and as the HEXOS diagnostic is a localized measurement 140° away from the injection site, there were concerns that variations in toroidal conductance and redeposition of material would add extra uncertainty to the measurement.

The summary of these conversions can be found in Table 1 which shows injection quantities estimated by QSV camera signals, relative injection quantities as determined by the HEXOS diagnostic, and the estimated range of injection quantities provided by these methods. We note again that we are not claiming a precise measurement of injection quantity, and that the ranges provides in the final table row represent the rough accuracy limits of this method. Injections in this discharge appear to fall into three categories as distinguished by both the estimated size of injection as well as their respective effects upon the discharge. The initial injections, prior to 4 s, are of quantities less than 10mg per pulse and do not appear to strongly perturb the plasma. During the next period of injections from 4 - 5 s, injected quantities between 10 and 20 mg per pulse are observed and a transient positive effect upon the plasma is recorded, with that effect having concluded prior to the next injection. For the final period of injections from 5 - 6.5s injection quantities above 20 mg are estimated and the net beneficial effects upon the plasma, while varying, continue throughout the pulse sequence until the final pulse triggers a radiative collapse of the discharge at $t = 6.2s$. Discussion of these injections and their subsequent effects upon the plasma will be covered in the next section.

This is the author's peer reviewed, accepted manuscript. However, the online version of record will be different from this version once it has been copyedited and typeset.

PLEASE CITE THIS ARTICLE AS DOI: 10.1063/5.0047274

Pulse Start (s)	2.1s	2.7s	3.0s	3.3s	3.6s	3.9s	4.2s	4.5s	4.8s	5.1s	5.4s	5.6s	5.9s	6.2s
QSV Pixel Counts	3.9E+6	2.7E+6	7.6E+6	1.2E+7	2.8E+7	2.0E+7	6.6E+7	4.6E+7	3.6E+7	1.0E+8	1.0E+8	1.1E+8	1.3E+8	1.9E+8
Injection quantity QSV (mg)	0.9	0.6	1.8	2.9	6.7	4.7	15.7	10.9	8.5	23.7	24.6	25.3	31.3	45.3
HEXOS Signal Intensity	50		91	92	358	315	849	616	434	1151	1146	1154	1592	2712
Injection quantity HEXOS (mg)	1.0		1.8	1.8	7.1	6.3	16.9	12.2	8.6	22.8	22.8	22.9	31.6	53.9
Estimated Injection Quantity	1 - 10 mg/pulse						10 - 20 mg/pulse			20 - 60 mg/pulse				

Table 1 : Estimation of injection quantities for experimental program 20180927-47. The top row indicates the start time of the pulse being analyzed while the next two rows are the integrated pixel intensities from the QSV cameras and that conversion into approximate mg quantities. The quantities in the third row are the integrated HEXOS signal for the same pulses while the 4th row is the relative injection quantity estimation arrived at by normalizing the initial pulse to 1mg. Given the uncertainties in this measurement method the final row represents the injection quantity range of the pulses we are utilizing for classification purposes.

Overall these experiments have shown the W7-X discharges to be continually robust to material injection at quantities up to 20 mg/pulse or 60 mg/sec. At these levels of externally applied heating (4MW ECRH) the plasma is able to subsume and then expel the injected powder, returning to a baseline state prior to the next injection event as evidenced by only a marginal rise in Z_{eff} , to be shown in section 5.2. There are no indications that the plasma could not continue in this state for an extended period of time, suggesting that this level of material introduction could be utilized for future PFC conditioning studies. For injections larger than 20mg/pulse the plasma does not return to a baseline state between pulses and the continued injection of material leads to an impurity buildup and the expected radiative collapse for this discharge. We note that as a consequence of the rapid plasma termination at the end of the injection series, the full boron carbide load from the final injection pulse was not assimilated into the plasma. This resulted in a mobilization of incompletely ablated material during the start-up of the subsequent discharge and an

additional radiative collapse. This effect was limited to the next discharge and subsequent operations were conducted without noted deleterious effect from the PMPI injections.

3.3. Injection effects on plasma behavior

Our discussion focuses on the results obtained during W7-X experimental program 20180927-47, the overall behavior of which can be seen in figure 10. While the effects noted here can be observed in the other B₄C injection experiments to a lesser extent, this was the only discharge subject to injections larger than 10 mg/pulse. In addition, the range in pulse sizes allows a direct comparison of the effects of multiple injection quantities on plasma behavior within the same discharge.

The smallest injections which occur in the period from 2.5 - 4s produce mild transient increases in the radiated power and density, as observed in the top two panels of figure 10. These injections do not appear to result in substantial changes to either the core electron or ion temperature resolvable among the nominal signal variations and only result in minor depressions in the overall plasma stored energy. The perturbations to all signals return to a baseline level in the time between injection events. We also note that the ECRH probes do not report a significant reaction of non-absorbed power due to material injection and thus the absorbed ECRH power (P_{ECRH}) is nominally constant over the course of the experimental program.

The series of moderate injections from 4.1s to 5.2s generate more substantial modifications to overall behavior and will be used to explore the demonstrated and repeatable effects upon the plasma. The radial profiles of the ion and electron temperatures as well as the electron density, at the times highlighted by the colored dashed lines in figure 10, are shown in figure 11. The dashed black trace corresponds to a pre-injection time of 2.08s and is the baseline to which future profiles are compared. The profiles corresponding to times $t = 4.18\text{s}$ and $t = 5.08\text{s}$ are taken during the initial mass incursion phase of the PMPI pulses. Upon injection into the plasma, the incident material is ablated by electrons rapidly free streaming along the field lines. Because of the long connection lengths present in the W7-X stellarator these electrons draw energy from large sections of the edge plasma, thus rapidly equilibrating the temperature along the edge flux surfaces. The energy utilized for ionization in the edge causes core electron heat losses leading to the observed reduction in core electron temperature (T_e) seen in both the third panel of figure 10 and the blue and green profiles shown in panel b) of figure 11. Also observed is a rise in the edge electron density (n_e , figure 11) and a loss of overall stored energy (W_{DIA}). The interplay of

these effects for the injection at $t = 5.07\text{s}$ is highlighted by the expanded panel on the right of figure 10. Strong increases in the observed radiated power and spikes in the boron-V HEXOS[43] signal also occur in conjunction with the incorporation of the injected boron carbide into the plasma. For these moderate injections we observe that the ion temperatures remain at the baseline levels during the initial phase of the injection event.

Once the material is fully integrated into the plasma, the radiated power and boron signal intensity return to near baseline levels. For reasons we will explore in the next section, during this post injection phase as denoted by the $t = 4.38$ and $t = 4.68$ traces in figure 11, there is a strong increase in the core ion temperature as well as a more moderate increase in the electron temperatures above the pre-injection level. The peak core ion temperatures are increased above the baseline temperatures by greater than 30% from a nominal value of 1.7 keV prior to granule injection to a maximum of 2.2-2.3 keV. The fact that the ion temperatures display a slower response to the injections indicates that the observed variations may themselves be a reaction to the previously enumerated changes in plasma parameters (n_e , T_e), rather than a direct consequence of material injection.

There is also a strong response exhibited by the stored energy (W_{DIA} , figure 10, 4th panel)[42]. While the stored energy decreases promptly with the introduction of material, during the recovery phase it is observed to exceed the pre-injection value. Examining the expanded section on the right hand side of figure 10 we can see that approximately 100ms after an injection event W_{DIA} has recovered to a pre-injection level. At this point, instead of remaining at the baseline level, it continues to increase for an additional 150ms to a level up to 30% larger than the initial value. For moderate injections, this increase in stored energy can then be seen to roll over and begin to decay back to the nominal discharge stored energy prior to the next injection event. The increase in stored energy cannot be simply attributed to an increase in density as the expanded panels show the stored energy reaching a peak even as the density has returned to near nominal quantities. The profiles corresponding to $t = 4.88\text{s}$ display the plasma state observed just 50ms after a more modest injection. As shown, the electron temperature is mildly raised however, unlike the traces from 150 ms after the larger injections, there is not yet a corresponding strong rise in the core ion temperature.

Transitioning to the period of largest injections from 5 – 6.5s, we note that in addition to the prompt responses there are also sustained effects to the overall plasma behavior. In figure 12 we show the electron temperature and density profile responses to a series of injections. The black trace in the first

panel is indicative of a pre-injection electron temperature profile taken at $t = 2.08$ s. The change from this profile to the one just after a pulsed powder injection can be seen in the difference between the red and black traces in panels a) and b). In panel a) the red trace, corresponding to a measurement at $t = 5.08$ s is taken just after the peak of an injection event. The exact timing of the pulse with respect to the measurement time can be seen in the HEXOS signal of the 4.85 nm B-V emission line at the bottom of the figure. Similar to the moderate size injections, there is a reduction in electron temperature as the injected material enters the discharge. The electron temperature remains depressed as the boron is assimilated into the discharge at $t = 5.18$ s trace, before rebounding to a level higher than the previous baseline level as $t = 5.28$ s trace with the core electron temperatures now observed at 3.5 keV as opposed to the 3.15 keV recorded before the series of injections began. In panel b) the incoming pulse is observed to generate a profile with increased edge density as the material is absorbed. Note that when comparing the early injection time (red) to the baseline pre-injection levels (black) we see that there is no change in core density during the early injection time periods consistent with the outside-in absorption of material. The later time traces show a relaxation of the steep edge gradient as the material is transported into the core at $t = 5.18$ s and $t = 5.28$ s. This evolution of the electron temperature is repeated in panels (c) and (e) for the two subsequent B_4C injections. Again we observe a suppressed core electron temperature as the material is injected and absorbed with a rebound of core performance once the boron has been fully integrated into the plasma.

Examining the three red traces in panels (b), (d), and (e) of figure 12 we observe the plasma relaxation from the induced flat profile as the material is assimilated. Density profile n_e (panel b) ($t = 5.08$ s) occurs 15 ms after the leading edge of the boron trace is recorded and is peaked at $\rho \approx 0.8$. The panel d) density profile at $t = 5.38$ s, recorded 30 ms after the B-V leading edge, shows that the profile has now flattened. The third set of density profiles traces (panel f) begins with a trace at $t = 5.68$ s which occurs 70 ms past the B-V leading edge. This profile shows a return to the standard peaked density profile as the edge has absorbed and either flushed or transmitted to the core the majority of the boron pulse with just a remnant of the electron density shown between the $t = 5.68$ s trace (red) and the other traces in the panel. In closely examining the behavior of the intermediate $t = 5.78$ s (green) trace we also note that the density profile appears to relax to the baseline behavior also in an outside-in manner with the edge matching the late time profile before the profile at the center of the discharge responds.

Elevations of the ion temperature in response to large material injections exceed those of the moderate injections as previously discussed. As shown in the 2-D profile evolutions in figure 13, the moderate pulses

prior to 5s are capable of generating performance improvements, in some cases exceeding the empirical limit of 1.8 keV observed during the majority of W7-X discharges[1]. These improvements are transitory, lasting at most 250 ms, roughly the interval between pulses, prior to a return to the discharge baseline state. However, once the injection quantity becomes large ($>20\text{mg}$) after $t = 5\text{s}$, the plasma no longer completely returns to a baseline state between injections. Thus, while the peak ion temperature is reduced due to the subsequent injection, the gains resulting from the previous injection are not completely diminished resulting in the core ion temperature being driven to a new peak height during each subsequent enhanced confinement phase. These evolutions are captured in the ion temperature profiles comprising panels b) - d) with the measurement time called out by the colored boxes on the bottom of the diamagnetic energy trace in panel e). As a unique feature of this graph series, the final time trace in a previous panel (for example $t = 5.38\text{s}$) is repeated in the panel below to facilitate a better comparison between injection pulses. This feature illustrates that the ion temperature which is elevated in an earlier pulse serves as a basis from which the next pulse builds.

The single slice ion temperature profile fits shown here are constrained by the electron temperature in the edge to remove condition whereby the ion temperature exceeds the electron temperature in these electron-only heated plasmas. The profiles are also flattened in the core to correct for elevated core temperature inversions due to low signal driven by the fast time resolution needed to resolve fine scale features. Thus while the 2D trace of the inverted XICS data does display instances of the measured core T_i values greater than 3 keV, because of these constraints on the analyzed profile slices we only claim a performance boost to 2.6 keV.

4. Discussion

During the majority of the standard ECRH powered discharges which comprise the bulk of W7-X operations during OP1.1 and 1.2[57, 1] T_e was observed to be substantially larger than T_i with a flat core density profile and a generally positive core radial electric field indicating electron root confinement[58, 46]. Noted in these experiments was the observation of an empirical limit to the core ion temperatures of approximately 1.8keV suggesting anomalous loss mechanisms and transport roughly an order of magnitude larger than the W7-X optimized neoclassical transport levels[59, 60]. Within the present operational space we expect that the three primary candidate modes which could be responsible for the turbulent transport are the Electron Temperature Gradient (ETG), Ion Temperature Gradient (ITG), and

Trapped Electron Modes (TEM) [61]. Gyrokinetic simulations[62] have shown that the W7-X three dimensional geometry prevents significant transport from the electron scale ETG modes[63] while the fact that the longitudinal invariant “J” displays a maximum value on the magnetic axis, the so called “maximum-J property”[64] means that the trapped electrons are localized into regions of good curvature[65]. This leaves micro instabilities, driven by the presence of a strong ITG band, and unstable under normal W7-X operational conditions[66, 67], as a proposed mechanism to explain the anomalous losses and thus the empirical limitation to the core ion temperatures.

There are however, some instances where the observed ion temperature limit has been exceeded. The most studied of these has been pellet enhanced discharges[68-70]. In the period following the injection of a stream of frozen hydrogen pellets into W7-X plasmas an elevation of core ion temperatures above 3 keV is recorded, with overall energy confinement temporarily surmounting the ISS04 scaling. The improvement in transport is consistent with a stabilization of the previously enumerated ITG turbulence[71] as a result of strongly peaked density profiles caused by deep fueling from the pellet train injection. This temporary stabilization reduces anomalous transport and increases the overall plasma stored energy leading to a reversal of the core radial electric field as the plasma transitions from electron to ion root.

These performance parameters are observed to be grossly similar to those observed during the post injection phases of the PMPI discharges and thus may suggest similar nascent causes. The effects of B₄C Injection into the W7-X plasma contain 2 distinct stages. The first stage is described by a change in the electron temperature and density profiles in response to the injection while the second stage is characterized by the plasma response to these modified profiles and results in increases to the ion temperature and overall discharge stored energy as well as confinement time. Having covered the first stage in the previous section, we turn to the second stage of the injection event.

4.1. Modification of plasma gradients and turbulence suppression

The initiation of the enhanced confinement period starts with the evolution of the density profiles. The ablation and ionization of the newly introduced material leads to a substantial increase in edge electron density. For example, a 10 mg pulse contributes a localized influx of up to 4.4×10^{20} boron and 1.1×10^{20} carbon atoms if fully integrated into the plasma. These contributions effect not just the magnitude, but

also the shape of the resultant profiles. This can be seen in the modification of profile gradients displayed in the left hand panels (a, c, and e) of figure 14. The major variations observed over the course of injection are to the density gradient. During the initial mass assimilation phase the edge density for $\rho > 0.8$ is strongly steepened which leads to a much flatter density throughout the core. However once this phase has completed the density gradient is steepened over the entire radial profile of the plasma. Periods of greatest enhanced confinement at $t = 5.28s$ also coincide with times of enhanced ion temperature gradients from $\rho = 0.8$ to $\rho = 0.4$. Experiments detailing enhanced performance of W7-X plasmas after pellet injection have also noted the most efficient turbulence stabilization to occur when steep density and temperature gradients are found to radially overlap[70] in support of the hypothesis of transiently stabilized ITG modes..

The changes in normalized inverse scale length, defined by $|a/L_{ne}| = a * |\nabla_r(n_e)|/n_e$, $|a/L_{Te}| = a * |\nabla_r(T_e)|/T_e$ and $|a/L_{Ti}| = a * |\nabla_r(T_i)|/T_i$ for minor radius $a = 0.5m$ are shown in the corresponding right hand side panels b), d), and f) of figure 14. The strongly reduced gradient scale length during the injection phase moves the plasma deeper into the so called "stability valley"[64] which occurs at conditions unfavorable for ITG and TEM growth[72] and this movement in turn drives a decrease in anomalous transport levels.

A consequence of this transition should be observable as a reduction in the presence of turbulent microstructures within the plasma. The measurement shown in figure 15 displays just such a reduction in the radially resolved density fluctuations during the post-powder injection periods (open markers) when compared to the pre-injection baseline(filled markers). This suggests a suppression of turbulence and thus a subsequent reduction in anomalous transport. We assert that following the recovery of the electron temperature, after the injected material has been ablated, ionized and thermalized, this reduction in transport allows for an extended electron-ion collisional interaction time which is most likely responsible for the observed higher ion temperatures given that the only heating for this plasma is delivered through ECRH.

4.2. Ambipolar electric field reversal and enhanced plasma confinement

The species specific radial flux which occurs within the stellarator geometry as a consequence of the ambipolarity condition[73] results in the neoclassical self generation of a radial electric field. In the

majority of W7-X ECRH heated plasmas, where $T_e \gg T_i$, this results in a positive radial electric field in the plasma core and the observation therein of the so called “electron-root” confinement[46]. However, during the enhanced confinement periods observed in the PMPI discharges the gap between core electron and ion temperature drops from 1.4 keV before injection to a minimum of 500 eV primarily due to an increase in ion temperature. As a consequence of these increased ion temperatures there is an observed reversal of the radial electric field corresponding to the “ion-root” solution of the ambipolarity relation[74] as displayed in figure 16. In panel a), the radial electric field as measured by the XICS is observed to be positive in the plasma core during the period before injection and has transitioned to a negative electric field as recorded after assimilation of the injected material. Examining the time history of the electric field as shown in panel b) clear indications of core ion root confinement occur coincident with the instances of enhanced performance. This measurement of the radial electric field is corroborated by a similar results recorded by the Doppler Reflectometer(DR). As with the XICS, a measurement of the perpendicular rotation velocity is utilized to determine electric field and the result is displayed panel c) of figure 16. As is shown, the radial electric field during periods of post-injection enhanced confinement is more strongly negative than is observed during the periods prior to injection. Note that the values presented in the figure are normalized by $E_r/\nabla r$ from the recorded data to account for the flux surface compression at the bean shaped outboard midplane location of the Doppler Reflectometer. Examining the XICS and DR traces we note that similar normalized radii for the two measurements are in generally good agreement in shape and in value to within a factor of 2. For example, the primary negative peak of the DR measurement at $\rho = 0.6$ is coincident with a strong negative swing of the XICS measurement at this value prior to the error bars of the XICS becoming large due to the lack of highly ionized argon in these outer radii. Similarly, the pre-injection values for the XICS and DR are slightly negative and essentially flat from $\rho = 0.6$ to $\rho = 0.3$. The positive swing evidenced by the XICS in the core region of the plasma is not resolved in this measurement by the DR.

The projected neoclassical ambipolar radial electric field can be calculated by solving the drift kinetic equation for a given set of temperature and density profiles. A comparison of this with the XICS radial electric field measurement as done in [48] shows good agreement over a significant portion of the W7-X operational space. To compare current measurements with theory, a neoclassical calculation of the electric field utilizing the SFINCS(Stellarator Fokker-Planck Iterative Neoclassical Conservative Solver[75]) code. For these calculations, the ion temperature measurements from the XICS diagnostic as well as the electron temperature and density measurements from Thomson scattering are used as inputs to generate

a numerical solution of the drift-kinetic equation for the species specific distribution function generating neoclassical fluxes and flows. The results of the electric field portion of the calculation, as displayed in panel d) figure 16 show that the depression of the electric field in response to the modified electron and ion temperature and density profiles is consistent with the underpinnings of neoclassical theory. While this calculation and the corresponding two measurements do not match exactly (note the difference in vertical scale between panel a) and panels c) and d)), there is good general agreement on the ability of the powder injection and the resulting changes in plasma profiles to significantly modify the radial electric field.

In these experiments, both E_r and E_r -shear may have an impact in the stabilization of density fluctuations. As shown in figure 15 and panel c) of figure 16, the reduction in the density fluctuations is measured in the radial range where the E_r -shear increases ($\rho \approx 0.4$ - 0.9) which points to the stabilizing effect of the E_r -shear as a relevant player. This effect however does not exclude the stabilizing effect of the E_r itself that can be relevant particularly in stellarators. This has been shown in Ref. [71], where the impact of the E_r on turbulence was studied using the gyrokinetic code GENE for W7-X configuration. These simulations show how E_r produces a displacement of the fluctuations in the magnetic surface towards regions with lower curvature less favourable for turbulence generation with the subsequent reduction in the turbulent transport.

Further evaluation of neoclassical energy flux in both the electron and ion root phases shows an amplified ion energy flux during periods of ion-root confinement significant enough that ions become the dominant neoclassical loss channel[48]. This is also consistent with a reduction in anomalous losses from turbulent transport and manifests as a transient increase in the stored energy. Given that the input ECRH power was maintained at a constant level over the course of the injection series this indicated a period of enhanced confinement. An average confinement time of 130ms is observed during the pre-injection period from 1-2 s as shown in figure 17. While this value then oscillates in response to the injections, the experimental energy confinement time, $\tau_E^{\text{exp}} = W_{\text{dia}} / (P_{\text{ECRH}} - dW_{\text{dia}}/dt)$, can be seen to reach values of 210ms during periods of enhanced confinement. These periods are also notable as they clearly surmount the values predicted by the ISS04 empirical scaling also shown in the figure. We note here that as the ISS04 scaling is intended as a metric for performance of stationary plasma conditions, a strict comparison to the transient elevations of the PMPI discharge is not completely tractable. However given that the periods of

enhanced confinement are on the order of a confinement time and thus could be considered quasi-stationary we offer the comparison as a figure of merit.

4.3. Additional Observations

As to be expected, the introduction of increasing levels of B₄C impurities generated a marked change in the effective ion charge (Z_{eff}). As shown in figure 18, small injections (< 10 mg) have little impact with impurity flushing completed in the interval between pulses allowing the plasma to return to a baseline state. The effective ion charge increases from approximate 1.3 at the beginning of the discharge to an elevated secondary plateau near 2 during the period of medium injection quantities from 4 – 5 s. For injections larger than 20mg/pulse the Z_{eff} measurement continues to increase with each subsequent pulse reaching an average of 3.5 with oscillations due to impurity injections and their subsequent flushing. It is only through repeated pulses of increasing magnitude that we reach a point whereby the discharge is no longer able to support the impurity burden at the present input power and the discharge suffers a radiative collapse.

The primary impurity species within the discharge; boron, carbon and oxygen respectively, are shown in the three lower panels, highlighting inter-pulse variations and changes in the overall baseline level. The given signal values are based on a Simpson integration over the line peaks with a local linear background subtraction. As such, signal levels can not be compared between any two lines, but each line shows the correct run of its individual signal level with the influence of neighboring lines reduced by the local background subtraction. There is a general increase in the boron signal as the injection quantity increases with the stepwise increment a direct consequence of the periodic injections from the PMPI and the inability of the discharge to completely flush that quantity of impurities prior to the next pulse. However, we note that there is not a corresponding increase in the carbon baseline level which is concomitantly introduced as a component of the boron carbide molecule. This may be due to the fact that while the PMPI injections are the primary contributor of B into these plasmas, the local graphite tiles provide a substantially larger C source than is generated by the injections. While only the carbon V line intensity is displayed, similar behavior has been noted over the ionization species from C-II to C-VI. Contrasting these signals is the observed decrease in overall oxygen signal intensity once the pulsed impurity injections begin, as shown in the bottom trace, the oxygen level at the end of the pulse sequence is roughly half of

the pre-injection intensity level. This overall behavior is observed with varying degrees in the ionization species from O-III through O-VI but with minimal response from the O-VII signal.

As the PMPI experiments were also intended to provide a first estimation of the efficacy of an Impurity Powder Dropper as an alternate means of wall conditioning for W7-X, spectroscopic data were scrutinized for evidence of wall conditioning. The expectations to generate conditioning effects were low due to the sustained discharge improvements observed by W7-X as a result of the standard boronizations. The observation that the plasma improvements resulting from a gaseous boronization did not appear to degrade significantly during the experimental operations conducted between the three boronizations could indicate that there was still an effective deposition layer on the plasma facing components. This would then mitigate any observable impact from additional material deposition. As such it was unsurprising that an attempt to determine a positive impact on wall conditioning as directly provided by the PMPI was inconclusive. At this juncture, all that can be stated with certainty is that the operation of the PMPI did not have a deleterious impact on the overall wall conditions or on subsequent experiments during OP1.2b. Absent the installation of a full IPD system, an adequate assessment of the powder injection effects by the PMPI on wall conditioning might best be accomplished by a dedicated set of PMPI experiments in either an unboronized machine or one far from a standard boronization..

In addition we also note that the high material fluence experiments were only attempted in the standard 5/5 magnetic configuration. In this configuration, a flux tube followed along any of the the 5 topologically distinct individual magnetic islands will return to its original location after a single toroidal transit. Replicating the PMPI experiments in both high (5/4) and low iota (5/6) rotational transform configurations might lead to greater contact between the initial injection site and a variety of plasma facing surfaces as these magnetic geometries are comprised of a single island chain transiting the vessel multiple times before returning to its original location. These configurations provide an extended connection length between the injection location and a plasma facing surface[26], and thus the impurity loaded island chain would have greater access to a range of limiter and divertor surfaces. These configurations and the respective changes in material transport as a result of the altered magnetic fields could be an interesting aspect of future experiments and would also allow correlation to recent results from full torus modeling of IPD boron injections at LHD[76] and DIII-D[77] which predicted asymmetries in the SOL impurity density accumulation and emission as well as material deposition.

5. Summary

The PMPI was successfully tested during the recent W7-X operation campaign with a demonstrated ability to inject on demand boron carbide pulses displaying good particle entrainment and unexpected effects on overall discharge behavior. Particles were horizontally injected at a range of pulse injection quantities from less than 1 mg up to at least 30 mg as determined by an in-situ measurement of local ablation characteristics. Wide angle cameras show rapid ablation of the injected particles and entrainment of impurity loads into field aligned flux tubes transiting the vessel. Observations of carbon filtered divertor imaging show direct engagement of injected material with high flux plasma facing surfaces allowing for the possibility of depositional coating. This, coupled with the observation that deposited boron tends to migrate around the vessel during normal plasma operation[1] provides support for the utilization of a single source of particulate injection to effectively distribute material throughout the vacuum vessel. In addition, by providing an array of injection events we are able to demonstrate a sustainable impurity burden for present W7-X experimental programs providing a baseline for future conditioning efforts.

Injected impurities are observed to enter the confined region of the discharge as evidenced by an increase in overall radiated power as well as increases in plasma density and measured Z_{eff} . Prompt response to injection also includes a reduction in electron temperature, a decrease in stored energy and an increase in spectroscopic boron intensity as the injected material is absorbed and thermalized. However, once the estimated injection quantity exceeds approximately 10 mg/pulse, there are more substantial effects upon the plasma behavior. Once the material has been assimilated into the discharge, there is an observed increase in ion temperature and stored energy. For moderate injection sizes, the duration of these effects is contained to the times between the individual pulses and so do not appear to generate cumulative effects whereas the larger injections (<20mg) generate a sustained increase in the core ion temperature. The accompanying increase in stored energy also continues to trend upward until the point where it is abruptly terminated by the subsequent introduction of an additional pulse of boron carbide, leading to radiative collapse.

The presumed sequence of events leading to these enhanced confinement periods proceeds as follows. The injection of the boron carbide powder depresses the electron temperature and shifts the location of density gradient. While unconfirmed during PMPI injection discharges, gyrokinetic simulations[71] of turbulence reduction via electron density peaking are supportive of the postulate that these conditions

lead to a reduction of the anomalous transport thus providing an extended time for electron-ion temperature equilibration resulting in increased ion temperatures. The reduction in temperature gap between the electrons and ions is then responsible for the reversal of the ambipolar electric field, transitioning the core of the plasma from an electron root to ion root confinement which in turn provides greater confinement and stored energy. A subsequent burst of powder eliminates this enhanced confinement by rapidly exhausting energy through the electron channel during material ablation. As such no definitive statement can be made about the expected lifetime of the enhanced confinement mode. It is assumed that the enhanced confinement will degrade as the density gradient decays leading to a return of greater anomalous transport and a loss of high temperature ions returning the ambipolar electric field to its nominal ECRH driven state.

In conclusion, we assert that systematic experiments with the PMPI could help determine if the utilization of a powder dropper as a real time conditioning technique would support the W7-X goals by assisting in the maintenance of premium wall conditions over the course of extreme long pulse (20 min+) discharges. Given the strong, but transient enhanced performance metrics generated during boron carbide injection discharges, we also believe that a more thorough investigation of these parameters could be a strong candidate for future investigation. As such, the ability of particle injection to maintain premium wall conditioning and possibly aid in plasma performance through profile shaping could certainly be viewed as a cooperative asset in future W7-X high performance long pulse campaigns.

6. Acknowledgements

This research was supported by the U.S. DOE under Contract No. DE-AC02-09CH11466 with Princeton University. This work has been carried out within the framework of the EUROfusion Consortium and has received funding from the Euratom research and training programme 2014-2018 and 2019-2020 under grant agreement No 633053. The views and opinions expressed herein do not necessarily reflect those of the European Commission.

7. Digital Data Statement

The data that support the findings of this study are available from the corresponding author upon reasonable request.

This is the author's peer reviewed, accepted manuscript. However, the online version of record will be different from this version once it has been copyedited and typeset.

PLEASE CITE THIS ARTICLE AS DOI: 10.1063/5.0047274

8. References

1. T. Klinger, T. Andreeva, S. Bozhnikov, C. Brandt, R. Burhenn, B. Buttenschön, G. Fuchert, B. Geiger, O. Grulke, H.P. Laqua, N. Pablant, et al "Overview of first W7X high performance operation" 2019 Nucl. Fusion **59** 112004
2. J Huang, X Gong, A M Garofalo, J Qian, J Chen, M Wu, M Li, Q Yuan, L Wang, C Pan, X Lin, Q Yang, A Ekedahl, R Maingi, C T Holcomb, E Li, L Zeng, B Zhang, J F Chang, X J Zhang, M Goniche, Y Peysson, X Zhu, Y Sun, G Xu, Q Zang, L Zhang, H Liu, B Lyu, R Ding, Q Ren, B Ding, W Guo, S Ding, N Xiang, Y Liang, F Liu, Y Zhao, B Xiao, J Hu, C Hu, L Hu, X Gao, P Fu, Y Song, X D Zhang, V Chan, J Li, B Wan and the EAST team "Progress of physics understanding for long pulse high-performance plasma on EAST towards the steady state operation of ITER and CFETR" 2020 Nucl. Fusion **62** 014019
3. H.K. Park, M.J. Choi, S.H. Hong, Y. In, Y.M. Jeon, J.S. Ko, W.H. Ko, J.G. Kwak, J.M. Kwon, J. Lee, J.H. Lee, W. Lee, Y.B. Nam, Y.K. Oh, B.H. Park, J.K. Park, Y.S. Park, S.J. Wang, M. Yoo, S.W. Yoon, J.G. Bak, C.S. Chang, W.H. Choe, Y. Chu, J. Chung, N. Eidietis, H.S. Han, S.H. Hahn, H.G. Jhang, J.W. Juhn, J.H. Kim, K. Kim, A. Loarte, H.H. Lee, K.C. Lee, D. Mueller, Y.S. Na, Y.U. Nam, G.Y. Park, K.R. Park, R.A. Pitts, S.A. Sabbagh, G.S. Yun and the KSTAR Team "Overview of KSTAR research progress and future plans toward ITER and K-DEMO" 2019 Nucl. Fusion **59** 112020
4. Y. Yoshimura, H. Kasahara, M. Tokitani, R. Sakamoto, Y. Ueda, S. Ito, K. Okada, S. Kubo, T. Shimoizuma, H. Igami, H. Takahashi, T.I. Tsujimura, R. Makino, S. Kobayashi, Y. Mizuno, T. Akiyama, N. Ashikawa, S. Masuzaki, G. Motojima, M. Shoji, C. Suzuki, H. Tanaka, K. Tanaka, T. Tokuzawa, H. Tsuchiya, I. Yamada, Y. Goto, H. Yamada, T. Mutoh, A. Komori, Y. Takeiri and the LHD Experiment Group "Progress of long pulse discharges by ECH in LHD" 2016 Nucl. Fusion **56** 046005
5. C. Bourdelle, J.F. Artaud, V. Basiuk, M. Bécoulet, S. Brémond, J. Bucalossi, H. Bufferand, G. Ciraolo, L. Colas, Y. Corre, X. Courtois, J. Decker, L. Delpech, P. Devynck, G. Dif-Pradalier, R.P. Doerner, D. Douai, R. Dumont, A. Ekedahl, N. Fedorczak, C. Fenzi, M. Firdaouss, J. Garcia, P. Ghendrih, C. Gil, G. Giruzzi, M. Goniche, C. Grisolia, A. Grosman, D. Guilhem, R. Guirlet, J. Gunn, P. Hennequin, J. Hillairet, T. Hoang, F. Imbeaux, I. Ivanova-Stanik, E. Joffrin, A. Kallenbach, J. Linke, T. Loarer, P. Lotte, P. Maget, Y. Marandet, M.L. Mayoral, O. Meyer, M. Missirlian, P. Mollard, P. Monier-Garbet, P. Moreau, E. Nardon, B. Pégourié, Y. Peysson, R. Sabot, F. Saint-Laurent, M. Schneider, J.M. Travère, E. Tsitrone, S. Vartanian, L. Vermare, M. Yoshida, R. Zagorski and JET Contributors "WEST Physics Basis" 2015 Nucl. Fusion **55** 063017
6. Thomas Härtl, Aleksander Drenik, Michael Kircher, Volker Rohde, Franz Stelzer, Wolfgang Zeidner, and the ASDEX Upgrade team "Optimization of the ASDEX Upgrade glow discharge" 2017 Fusion Eng. Des. **124** 283-286
7. T. Wauters, D. Borodin, R Brakel, S Brezinsek, K J Brunner, J Buermans, S Coda, A Dinklage, D Douai, O Ford, G Fuchert, A Gorjaev, H Grote, A Hakola, E Joffrin, J Knauer, T Loarer, H Laqua, A Lyssoivan, V Moiseenko, D Moseev, J Ongena, K Rahbarnia, D Ricci, V Rohde, S Romanelli, S Sereda, T Stange, F L Tabarés, Lilla Vanó, O Volzke, E Wang, the ASDEX Upgrade Team, TCV Team, EUROfusion MST1 Team, W7-X Team, JT-60SA team and JET contributors "Wall conditioning in fusion devices with superconducting coils" 2020 Plasma Phys. Control. Fusion **62** 034002
8. V. Rohde, R. Dux, A. Kallenbach, K. Krieger, R. Neu, and the ASDEX Upgrade Team "Wall conditioning in ASDEX Upgrade" 2007 J. Nucl. Mater **363-365** 1369-1374
9. R. Brakel, A. Dinklage, J. Fellingner, G. Fuchert, H. Grote, R. König, H. Laqua, T. Stange, O. Volzke, G. Schlisio, U. Wenzel, D. Zhang, A. Gorjaev, T. Wauters, S. Brezinsek, V. Moiseenko, A. A. Belitskii "Strategy and Optimisation of Wall Conditioning at the Wendelstein 7-X Stellarator" Preprint: 2018 IAEA Fusion Energy Conf. (Gandhinagar, India, 22-27 October 2018 EX/P8-17
10. A. Nagy, A. Bortolon, D. M. Mauzey, E. Wolfe, E. P. Gilson, R. Lunsford, R. Maingi, D. K. Mansfield, R. Nazikian, and A. L. Roquemore "A multi-species powder dropper for magnetic fusion applications" 2018 Rev. Sci Instrum. **89(10)**:10K121

This is the author's peer reviewed, accepted manuscript. However, the online version of record will be different from this version once it has been copyedited and typeset.

PLEASE CITE THIS ARTICLE AS DOI: 10.1063/5.0047274

11. H.W. Kugel, M.G. Bell, H. Schneider, J.P. Allain, R.E. Bell, R. Kaita, J. Kallman, S. Kaye, B.P. LeBlanca, D. Mansfield, R.E. Nygren, R. Maingi, J. Menard, D. Mueller, M. Ono, S. Paul, S. Gerhardt, R. Raman, S. Sabbagh, C.H. Skinner, V. Soukhanovskii, J. Timberlake, L.E. Zakharov, the NSTX Research Team "Lithium coatings on NSTX plasma facing components and its effects on boundary control, core plasma performance, and operation" 2010 Fusion Eng. & Des. **85**(6) 865-873
12. R. Maingi, J.S. Hu, Z. Sun, K. Tritz, G.Z. Zuo, W. Xu, M. Huang, X.C. Meng, J.M. Canik, A. Diallo, R. Lunsford, D.K. Mansfield, T.H. Osborne, X.Z. Gong, Y.F. Wang, Y.Y. Li and EAST team., "ELM elimination with Li powder injection in EAST discharges using the tungsten upper divertor" 2018 Nucl. Fusion **58** 024003
13. Z. Sun, A. Diallo, R. Maingi, Y.Z. Qian, K. Tritz, Y.F. Wang, Y.M. Wang, A. Bortolon, A. Nagy, L. Zhang, Y.M. Duan, Y. Ye, H.L. Zhao, H.Q. Wang, X. Gu, G.Z. Zuo, W. Xu, M. Huang, C.L. Li, X.C. Meng, C. Zhou, H.Q. Liu, Q. Zang, L. Wang, J.P. Qian, G.S. Xu, X.Z. Gong, J.S. Hu and EAST team, "Suppression of edge localized modes with real-time boron injection using the tungsten divertor in EAST" 2021 Nucl. Fusion **61** 014002
14. E. P. Gilson, H. H. Lee, A. Bortolon, A. Diallo, S. H. Hong, R. Maingi, D. Mansfield, A. Nagy, S. H. Park, S. W. Yoon, W. H. Choe, R. Nazikian, "Wall Conditioning and ELM Mitigation with Boron Nitride Powder Injection in KSTAR" 2021 Nucl. Mater. Energy submitted
15. F. Nespoli, N. Ashikawa, E.P. Gilson, R. Lunsford, S. Masuzaki, M. Shoji, T. Oishi, C. Suzuki, A. Nagy, A. Mollen, N.A. Pablant, K. Idab, M. Yoshinuma, N. Tamura, D.A. Gates, T. Morisaki and the LHD experiment group, "First impurity powder injection experiments in LHD" 2020 Nucl. Mater. Energy **25** 100842
16. A. Bortolon, V. Rohde, R. Maingi, E. Wolfrum, R. Dux, A. Herrmann, R. Lunsford, R.M. McDermott, A. Nagy, A. Kallenbach, D.K. Mansfield, R. Nazikian, R. Neu, and the ASDEX Upgrade team "Real-time wall conditioning by controlled injection of boron and boron nitride powder in full tungsten wall ASDEX Upgrade" 2019 Nucl. Mater. Energy **19** 384-389
17. A. Bortolon, R. Maingi, A. Nagy, J. Ren, J.D. Duran, A. Maan, D.C. Donovan, J.A. Boedo, D.L. Rudakov, A.W. Hyatt, T.W. Wilks, M.W. Shafer, C.M. Samuelli, M.E. Fenstermacher, E.P. Gilson, R. Lunsford, D.K. Mansfield, T. Abrams and R. Nazikian "Observations of wall conditioning by means of boron powder injection in DIII-D H-mode plasmas" 2020 Nucl. Fusion **60** 126010
18. R. Maingi, D.P. Boyle, J.M. Canik, S.M. Kaye, C.H. Skinner, J.P. Allain, M.G. Bell, R.E. Bell, S.P. Gerhardt, T.K. Gray, M.A. Jaworski, R. Kaita, H.W. Kugel, B.P. LeBlanc, J. Manickam, D.K. Mansfield, J.E. Menard, T.H. Osborne, R. Raman, A.L. Roquemore, S.A. Sabbagh, P.B. Snyder and V.A. Soukhanovskii, "The effect of progressively increasing lithium coatings on plasma discharge characteristics, transport, edge profiles and ELM stability in the National Spherical Torus Experiment" 2012 Nucl. Fusion **52** 083001
19. Z. Sun, R. Maingi, J.S. Hu, W. Xu, G.Z. Zuo, Y.W. Yu, C.R. Wu, M. Huang, X.C. Meng, L. Zhang, L. Wang, S.T. Mao, F. Ding, D.K. Mansfield, J. Canik, R. Lunsford, A. Bortolon, X.Z. Gong, and the EAST Team, "Real time wall conditioning with lithium powder injection in long pulse H-mode plasmas in EAST with tungsten divertor" 2019 Nucl. Mater. Energy **19** 124-130
20. R. Lunsford, V. Rohde, A. Bortolon, R. Dux, A. Herrmann, A. Kallenbach, R.M. McDermott, P. David, A. Drenik, F. Laggner, R. Maingi, D. K. Mansfield, A. Nagy, R. Neu, E. Wolfrum and the ASDEX Upgrade team, "Active conditioning of ASDEX Upgrade tungsten plasma-facing components and discharge enhancement through boron and boron nitride particulate injection" 2019 Nucl. Fusion **59** 126034
21. Tom Wauters, Andrei Gorjaev, Arturo Alonso, Juergen Balduhn, Rudolf Brakel, Sebastijan Brezinsek, Andreas Dinklage, Heinz Grote, Joris Fellingner, Oliver P. Ford, Ralf König, Heinrich Laqua, Dmitry Matveev, Torsten Stange, Lilla Vanó and the W7-X team, "Wall conditioning throughout the first carbon divertor campaign on Wendelstein 7-X" 2018 Nucl. Mater. Energy **17** 235-241
22. Andrei Gorjaev, T. Wauters, R. Brakel, S. Brezinsek, A. Dinklage, J. Fellingner, H. Grote, D. Moseev, S. Sereda, O. Volzke, and the W7-X Team, "Wall conditioning at the Wendelstein 7-X stellarator operating with a graphite divertor" 2020 Phys. Scripta **2020** 014063
23. S. Sereda, S. Brezinsek, E. Wang, T. Barbui, R. Brakel, B. Buttenschön, A. Gorjaev, U. Hergenrohn, U. Höfel, M. Jakubowski, A. Knieps, R. König, M. Krychowiak, S. Kwak, Y. Liang, D. Naujoks, A. Pavone, M. Rasinski, L.

This is the author's peer reviewed, accepted manuscript. However, the online version of record will be different from this version once it has been copyedited and typeset.

PLEASE CITE THIS ARTICLE AS DOI: 10.1063/5.0047274

- Rudischhauser, M. Ślęczka, J. Svensson, H. Viebke, T. Wauters, Y. Wei, V. Winters, D. Zhang and the W7-X team "Impact of boronizations on impurity sources and performance in Wendelstein 7-X" 2020 Nucl. Fusion **60** 086007
24. Alexander Nagy, A. Bortolon D. Gates E. Gilson, C. Killer, T. Klinger, R. Lunsford, R. Maingi, D. Mansfield, D. Mauzey, R. Nazikian, L. Roquemore, E. Wolfe, "A Horizontal Powder Injector for W7X" 2019 Fusion Eng. Des. **146.B** 1403-1407 <https://doi.org/10.1016/j.fusengdes.2018.12.099>
25. D. Nicolai, V. Borsuk, P. Drews, O. Grulke, K.P.Hollfeld, T. Krings, Y. Liang, Ch. Linsmeier, O. Neubauer, G. Satheeswaran, B. Schweer, G. Offermanns, and the W7-X Team "A multi-purpose manipulator system for W7-X as user facility for plasma edge investigation" 2017 Fusion Eng. Des. **123** 960-964
26. Carsten Killer, Olaf Grulke, Philipp Drews, Yu Gao, Marcin Jakubowski, Alexander Knieps, Dirk Nicolai, Holger Niemann, Aleix Puig Sitjes, Guruparan Satheeswaran and W7-X Team "Characterization of the W7-X scrape off layer using reciprocating probes" 2019 Nucl. Fusion **59** 086013 2019
27. R. Lunsford, A. Bortolon, A.L. Roquemore, D.K. Mansfield, M.A. Jaworski, R. Kaita, R. Maingi and A. Nagy "Multi-species impurity granule injection and mass deposition projections in NSTX-U discharges" 2017 Nucl. Fusion **57** 076008
28. R. Lunsford, A. Bortolon, R. Maingi, D. K. Mansfield, A. Nagy, G. L. Jackson, T. Osborne, "Supplemental ELM control in ITER through beryllium granule injection" 2019 Nucl. Mater. Energy **19** 34-41
29. Craig Beidler, Günter Grieger, Franz Herrnegger, Ewald Harmeyer, Johann Kisslinger, Wolf Lotz, Henning Maassberg, Peter Merkel, Jürgen Nührenberg, Fritz Rau, Jörg Sapper, Francesco Sardei, Ruben Scardovelli, Arnulf Schlüter & Horst Wobig "Physics and engineering design for Wendelstein VII-X" 1990 Fusion Sci. Tech. **17** 148-168
30. A. Dinklage, C. D. Beidler, P. Helander, G. Fuchert, H. Maaßberg, K. Rahbarnia, T. Sunn Pedersen, Y. Turkin, R. C. Wolf, A. Alonso, T. Andreeva, B. Blackwell, S. Bozhnikov, B. Buttenschön, A. Czarnecka, F. Effenberg, Y. Feng, J. Geiger, M. Hirsch, U. Höfel, M. Jakubowski, T. Klinger, J. Knauer, G. Kocsis, A. Krämer-Flecken, M. Kubkowska, A. Langenberg, H. P. Laqua, N. Marushchenko, A. Mollén, U. Neuner, H. Niemann, E. Pasch, N. Pablant, L. Rudischhauser, H. M. Smith, O. Schmitz, T. Stange, T. Szepesi, G. Weir, T. Windisch, G. A. Wurden, D. Zhang & and the W7-X Team, "Magnetic configuration effects on the Wendelstein 7-X stellarator" 2018 Nature Physics **14** 855-860
31. Y. Feng, F. Sardei, J. Kisslinger, P. Grigull, K. McCormick, D. Reiter, "3D edge modeling and island divertor physics" 2004 Contrib. Plasma Phys. **44** 57-69
32. Samuel A. Lazerson, Sergey Bozhnikov, Ben Israeli, Matthias Otte, Holger Niemann, Victor Bykov, Michael Endler, Tamara Andreeva, Adnan Ali, Peter Drewelow, Marcin Jakubowski, Aleix Puig Sitjes, Fabio Pisano, Barbara Cannas and the W7-X Team "Error fields in the Wendelstein 7-X stellarator" 2018 Plasma Physics and Controlled Fusion, **60**(12), 124002–12. <http://doi.org/10.1088/1361-6587/aee96b>
33. S. A. Lazerson, Yu Gao, Kenneth Hammond, Carsten Killer, Georg Schlisio, Matthias Otte, Christoph Biedermann, Monica Spolaore, Sergey Bozhnikov, Joachim Geiger, Olaf Grulke, Dirk Nicolai, Guruparan Satheeswaran, Holger Niemann, Marcin Jakubowski, Peter Drewelow, Aleix Puig Sitjes, Adnan Ali, Barbara Cannas, Fabio Pisano, Ralph König, Glen Wurden, Gabor Kocsis, Tamás Szepesi, Uwe Wenzel, Matthias Mulsow, Kian Rahbarnia, Jonathan Schilling, Ulrich Neuner, Tamara Andreeva, Henning Thomsen, Jens Knauer, Kai Jakob Brunner, Boyd Blackwell, Michael Endler, Soren Klose, Lukas Rudischhauser and the W7-X Team, "Tuning of the rotational transform in Wendelstein 7-X" 2019 Nuclear Fusion, **59**(12), 126004–12. <http://doi.org/10.1088/1741-4326/ab3df0>
34. Thomas Sunn Pedersen, Ralf König, Maciej Krychowiak, Marcin Jakubowski, Jürgen Baldzuhn, Sergey Bozhnikov, Golo Fuchert, Andreas Langenberg, Holger Niemann, Daihong Zhang, Kian Rahbarnia, Hans-Stephan Bosch, Yevgen Kazakov, Sebastijan Brezinsek, Yu Gao, Novimir Pablant and the W7-X Team "First results from divertor operation in Wendelstein 7-X" 2019 Plasma Phys. Control. Fusion **61** 014035
35. R. C. Wolf, A. Alonso, S. Äkäslompolo, J. Baldzuhn, M. Beurskens, C. D. Beidler, C. Biedermann, H.-S. Bosch, S. Bozhnikov, R. Brakel, H. Braune, S. Brezinsek, K.-J. Brunner, H. Damm, A. Dinklage, P. Drewelow, F. Effenberg, Y. Feng, O. Ford, G. Fuchert, Y. Gao, J. Geiger, O. Grulke, N. Harder, D. Hartmann, P. Helander, B. Heinemann, M. Hirsch, U. Höfel, C. Hopf, K. Ida, M. Isobe, M. W. Jakubowski, Y. O. Kazakov, C. Killer, T. Klinger, J. Knauer, R. König, M. Krychowiak, A. Langenberg, H. P. Laqua, S. Lazerson, P. McNeely, S. Marsen, N. Marushchenko, R. Nocentini, K.

This is the author's peer reviewed, accepted manuscript. However, the online version of record will be different from this version once it has been copyedited and typeset.

PLEASE CITE THIS ARTICLE AS DOI: 10.1063/5.0047274

- Ogawa, G. Orozco, M. Osakabe, M. Otte, N. Pablant, E. Pasch, A. Pavone, M. Porkolab, A. Puig Sitjes, K. Rahbarnia, R. Riedl, N. Rust, E. Scott, J. Schilling, R. Schroeder, T. Stange, A. von Stechow, E. Strumberger, T. Sunn Pedersen, J. Svensson, H. Thomson, Y. Turkin, L. Vano, T. Wauters, G. Wurden, M. Yoshinuma, M. Zanini, D. Zhang, and the Wendelstein 7-X Team "Performance of Wendelstein 7-X stellarator plasmas during the first divertor operation phase" 2019 Phys. Plasmas **26** 082504
36. F. Effenberg, H. Niemann, Y. Feng, J. Geiger, O. Schmitz, Y. Suzuki, A. Ali, T. Barbui, S. Brezinsek, H. Frerichs, M. Jakubowski, R. Konig, M. Krychowiak, A. Puig Sitjes, J.C. Schmitt, T. Sunn Pedersen, W7-X Team "Investigation of 3D effects on heat fluxes in performance-optimized island divertor configurations at Wendelstein 7-X" 2019 Nucl. Mater. Energy **18** 262-267
37. G J M Hagelaar, D Kogut, D Douai and R A Pitts "Modelling of tokamak glow discharge cleaning I: physical principles" 2014 Plasma Phys. Control. Fusion **57**(2) 025008
38. A. Gorjaev, T. Wauters, R. Brakel, H. Grote, M. Gruca, O. Volzke, S. Brezinsek, A. Dinklage, M. Kubkowska, U. Neuner "Development of glow discharge and electron cyclotron resonance heating conditioning on W7-X" 2019 Nucl. Mater. Energy **18** 227-232
39. S.A. Bozhnikov, M. Beurskens, A. Dal Molin, G. Fuchert, E. Pasch, M.R. Stoneking, M. Hirsch, U. Höfel, J. Knauer, J. Svensson, H. Trimiño Mora and R.C. Wolf "The Thomson scattering diagnostic at Wendelstein 7-X and its performance in the first operation phase" 2017 Journal of Instrumentation **12** P10004
40. E. Pasch, M.N.A. Beurskens S. A. Bozhnikov, G. Fuchert, J. Knauer, R.C. Wolf and W7-X Team "The Thomson scattering system at Wendelstein 7-X" 2016 Rev. Sci. Instrum. **87** 11E729
41. K.J. Brunner T. Akiyama, M. Hirsch, J. Knauer, P. Kornejew, B. Kursinski, H. Laqua, J. Meineke, H. Trimiño Mora and R. C. Wolf "Real-time dispersion interferometry for density feedback in fusion devices" 2018 Journal of Instrumentation, **13**, P09002
42. K. Rahbarnia, H. Thomsen, U. Neuner, J. Schilling, J. Geiger, G. Fuchert, T. Andreeva, M. Endler, D. Hathiramani, T. Bluhm, M. Zilker, B.B. Carvalho, A. Werner and Wendelstein 7-X Team "Diamagnetic energy measurements during the first operational phase at the Wendelstein 7-X stellarator" 2018 Nucl. Fusion **58** 096010
43. B. Buttenschön, R. Burhenn, M. Kubkowska, A. Czarnecka, T. Fornal, N. Krawczyk, D. Zhang, N. Pablant, A. Langenberg, P. Valson, H. Thomsen, W. Biel, J. Aßmann, the Wendelstein 7-X team, "Spectroscopic impurity survey in the first operation phase of Wendelstein 7-X" 2016 Proceedings of 43rd EPS Conference on Controlled Fusion and Plasma Physics, Leuven, Belgium, Vol. **40A**, P4.012
44. D. Hathiramani, A. Ali, G. Anda, T. Barbui, C. Biedermann, A. Charl, D. Chauvin, G. Czymek, C.P. Dhard, P. Drewelow, A. Dudek, F. Effenberg, G. Ehrke, M. Endler, D.A. Ennis, J. Fellingner, O. Ford, S. Freundt, D. Gradic, K. Grosser, J. Harris, H. Hölbe, M.W. Jakubowski, M. Knaup, G. Kocsis, R. König, M. Krause, T. Kremeyer, P. Kornejew, M. Krychowiak, H.T. Lambertz, H. Jenzsch, M. Mayer, S. Mohr, O. Neubauer, M. Otte, V. Perseo, D. Pilopp, L. Rudischhauser, O. Schmitz, B. Schweer, M. Schülke, L. Stephey, T. Szepesi, A. Terra, M. Toth, U. Wenzel, G.A. Wurden, S. Zolotnik, T. Sunn Pedersen, the W7-X Team, "Upgrades of edge, divertor and scrape-off layer diagnostics of W7-X for OP1.2" 2018 Fusion Engineering and Design Vol 136 Pg 304-308
45. R. König, J. Baldzuhn, W. Biel, C. Biedermann, H.S. Bosch, S. Bozhnikov, T. Bräuer, B. Brotas de Carvalho, R. Burhenn, B. Buttenschön, G. Cseh, A. Czarnecka, M. Endler, V. Erckmann, T. Estrada, J. Geiger, O. Grulke, D. Hartmann, D. Hathiramani, M. Hirsch, S. Jablonski, M. Jakubowski, J. Kaczmarczyk, T. Klinger, S. Klose, G. Kocsis, P. Kornejew, A. Krämer-Flecken, T. Kremeyer, M. Krychowiak, M. Kubkowska, A. Langenberg, H. P. Laqua, M. Laux, Y. Liang, A. Lorenz, A.O. Marchuk, V. Moncada, O. Neubauer, U. Neuner, J.W. Oosterbeek, M. Otte, N. Pablant, E. Pasch, T.S. Pedersen, K. Rahbarnia, L. Ryc, O. Schmitz, W. Schneider, H. Schuhmacher, B. Schweer, T. Stange, H. Thomsen, J.-M. Travers, T. Szepesi, U. Wenzel, A. Werner, B. Wiegel, T. Windisch, R. Wolf, G.A. Wurden, D. Zhang, A. Zimbal, S. Zolotnik and the W7-X Team, "The Set of Diagnostics for the First Operation Campaign of the Wendelstein 7-X Stellarator" 2015 Journal of Instrumentation **10** P10002
46. N. A. Pablant, A. Langenberg, A. Alonso, C. D. Beidler, M. Bitter, S. Bozhnikov, R. Burhenn, M. Beurskens, L. Delgado-Aparicio, A. Dinklage, G. Fuchert, D. Gates, J. Geiger, K. W. Hill, U. Höfel, M. Hirsch, J. Knauer, A. Krämer-Flecken, M.

This is the author's peer reviewed, accepted manuscript. However, the online version of record will be different from this version once it has been copyedited and typeset.

PLEASE CITE THIS ARTICLE AS DOI: 10.1063/5.0047274

- Landreman, S. Lazerson, H. Maaßberg, O. Marchuk, S. Massidda, G. H. Neilson, E. Pasch, S. Satake, J. Svensson, P. Traverso, Y. Turkin, P. Valsen, J. L. Velasco, G. Weir, T. Windisch, R. C. Wolf, M. Yokoyama, D. Zhang, and the W7-X Team, "Core electric field and transport in Wendelstein 7-X plasmas, 2018 Phys. Plasmas **25** 022508
47. N.A. Pablant, A. Langenberg, J. A. Alonso, M. Bitter, S. A. Bozhnikov, O. P. Ford, K. W. Hill, J. Kring, O. Marchuck, J. Svensson, P. Traverso, T. Windisch, Y. Yakusevitch, and W7-X Team, "Correction and verification of x-ray imaging crystal spectrometer analysis on Wendelstein 7-X through X-ray ray tracing" 2021 Review of Scientific Instruments **92**, 043530
48. N. Pablant, A. Langenberg, A. Alonso, J. Baldzuhn, C.D. Beidler, S. Bozhnikov, R. Burhenn, K.J. Brunner, A. Dinklage, G. Fuchert, O. Ford, D.A. Gates, J. Geiger, M. Hirsch, U. Höfel, Ye.O. Kazakov, J. Knauer, M. Krychowiak, H. Laqua, M. Landreman, S. Lazerson, H. Maaßberg, O. Marchuck, A. Mollen, E. Pasch, A. Pavone, S. Satake, T. Schröder, H.M. Smith, J. Svensson, P. Traverso, Y. Turkin, J.L. Velasco, A. von Stechow, F. Warmer, G. Weir, R.C. Wolf, D. Zhang and the W7-X Team "Investigation of the neoclassical ambipolar electric field in ion-root plasmas on W7-X" 2020 Nucl. Fusion **60** 036021
49. M Hirsch, E Holzhauer, J Baldzuhn, B Kurzan and B Scott, "Doppler reflectometry for the investigation of propagating density perturbations. 2001 Phys Plasma Confined Fusion **43** 1641
50. M. Hirsch, E. Holzhauer and H.-J. Hartfuss, "Reflectometry for Wendelstein 7-X" 2006 Nucl. Fusion, **46** 5853
51. P. Hennequin, C. Honoré, A. Truc, A. Quéméneur, N. Lemoine, J.-M. Chareau, R. Sabot, "Doppler backscattering system for measuring fluctuations and their perpendicular velocity on Tore Supra" 2004 Rev Sci. Instrum. **75** 3881
52. G. D. Conway, J Schirmer, S Klenge, W Suttrop, E Holzhauer and the ASDEX Upgrade Team¹ "Plasma rotation profile measurements using Doppler reflectometry "2004 Plasma Phys Control. Fusion **46** 951
53. T Happel, T Estrada, Emilio Blanco, Victor Tribaldos, A. Cappa, A. Bustos, "Doppler reflectometer system in the stellarator TJ-II" 2009 Rev Sci. Instrum. **80** 073502
54. D. Carralero, T. Estrada, T. Windisch, J.L. Velasco, J.A. Alonso, M. Beurskens, S. Bozhnikov, H. Damm, G. Fuchert, Y. Gao, M. Jakubowski, H. Nieman, N. Pablant, E. Pasch, G. Weir and the Wendelstein 7-X team "Characterization of the radial electric field and edge velocity shear in Wendelstein 7-X" 2020 Nucl. Fusion **60** 106019
55. Teresa Estrada, Daniel Carralero, Thomas Windisch, Edilberto Sanchez, José Manuel García Regaña, José Martínez, Angel de la Peña, Jose Luis Velasco, J Arturo Alonso, Marc N A Beurskens, Sergey A Bozhnikov, Hannes Damm, Golo Fuchert, Ralf Kleiber, Novimir Antoniuk Pablant and Ekkehard Pasch, "Radial electric field and density fluctuations measured by Doppler reflectometry during the post-pellet enhanced confinement phase in W7-X" 2021 Nucl. Fusion **61** 046008
56. G. Kocsis, T. Baross, C. Biedermann, G. Bodnár, G. Cseh, T. Ilkei, R. König, M. Otte, T. Szabolics, T. Szepesi, S.Zoletnik, "Overview video diagnostics for the W7-X stellarator" 2015 Fusion Eng & Design **96-97** 808-811
57. R.C. Wolf, A. Ali, A. Alonso, J. Baldzuhn, C. Beidler, M. Beurskens, C. Biedermann, H.-S. Bosch, S. Bozhnikov, R. Brakel, A. Dinklage, Y. Feng, G. Fuchert, J. Geiger, et al., "Major results from the first plasma campaign of the Wendelstein 7-X stellarator", 2017 Nucl Fusion **57** 102020
58. M. Hirsch, A. Dinklage, A. Alonso, G. Fuchert, S. Bozhnikov, U. Höfel, T. Andreeva, J. Baldzuhn, M. Beurskens, H.-S. Bosch, C.D. Beidler, C. Biedermann, E. Blanco, et al., "Confinement in Wendelstein 7-X limiter plasmas" 2017 Nucl. Fusion **57** 086010
59. A. Langenberg, N. A. Pablant, Th. Wegner, P. Traverso, O. Marchuk, T. Bräuer, B. Geiger, G. Fuchert, S. Bozhnikov, E. Pasch, O. Grulke, F. Kunkel, C. Killer, D. Nicolai, G. Satheeswaran, K. P. Hollfeld, B. Schweer, T. Krings, P. Drews, G. Offermanns, A. Pavone, J. Svensson, J. A. Alonso, R. Burhenn, R. C. Wolf, and the W7-X Team "Prospectus of X-ray imaging spectrometers for impurity transport: Recent results from the stellarator Wendelstein 7-X" 2018, Rev. Sci. Instrum **89** 10G101
60. B. Geiger, Th. Wegner, C.D. Beidler, R. Burhenn, B. Buttenschön, R. Dux, A. Langenberg, N.A. Pablant, T. Pütterich, Y. Turkin, T. Windisch, V. Winters, M. Beurskens, C. Biedermann, K.J. Brunner, G. Cseh, H. Damm, F. Effenberg, G. Fuchert, O. Grulke, J.H. Harris, C. Killer, J. Knauer, G. Kocsis, A. Krämer-Flecken, T. Kremeyer, M. Krychowiak, O.

This is the author's peer reviewed, accepted manuscript. However, the online version of record will be different from this version once it has been copyedited and typeset.

PLEASE CITE THIS ARTICLE AS DOI: 10.1063/5.0047274

- Marchuk, D. Nicolai, K. Rahbarnia, G. Satheeswaran, J. Schilling, O. Schmitz, T. Schröder, T. Szepesi, H. Thomsen, H. Trimino Mora, P. Traverso, D. Zhang and The W7-X Team "Observation of anomalous impurity transport during low density experiments in W7-X with laser blow-off injections of iron" 2019 Nucl. Fusion **59** 046009
61. A.v. Stechow, O. Grulke, Th. Wegner, J. H. E. Proll, J. A. Alcusón, H. M. Smith, J. Baldzuhn, C. D. Beidler, M. N. A. Beurskens, S. A. Bozhnikov, E. Edlund, B. Geiger, Z. Huang, O. P. Ford, G. Fuchert, A. Langenberg, N. Pablant, E. Pasch, M. Porkolab, K. Rahbarnia, J. Schilling, E. R. Scott, H. Thomsen, L. Vanó, G. Weir, and The W7-X Team "Suppression of core turbulence by profile shaping in Wendelstein 7-X" Phys. Rev. Lett. submitted 2021
62. G. G. Plunk, P. Xanthopoulos, G. M. Weir, S. A. Bozhnikov, A. Dinklage, G. Fuchert, J. Geiger, M. Hirsch, U. Hoefel, M. Jakubowski, A. Langenberg, N. Pablant, E. Pasch, T. Stange, D. Zhang, and the W7-X Team "Stellarators Resist Turbulent Transport on the Electron Larmor Scale" 2019 Phys. Rev. Lett. **122** 035002
63. J.M. Garcia-Regaña, M. Barnes, I. Calvo, F. I. Parra, J.A. Alcusón, R. Davies, A. González-Jerez, A. Mollén, E. Sánchez, J.L. Velasco, and A. Zocco "Turbulent impurity transport simulations in Wendelstein 7-X plasmas J. Plasma Phys. (2021) 87 855870103
64. J A Alcusón, P Xanthopoulos, G G Plunk, P Helander, F Wilms, Y Turkin, A von Stechow and O Grulke "Suppression of electrostatic instabilities in maximum J stellarators" 2020 Plasma Phys. Control. Fusion **62** 035005
65. P. Helander, J.H.E. Proll, G. G. Plunk "Collisionless microinstabilities in stellarators I - analytical theory of trapped-particle modes" 2013 Phys. Plasmas **20** 122506
66. P. Helander, T. Bird, F. Jenko, R. Kleiber, G.G. Plunk, J.H.E. Proll, J. Riemann and P. Xanthopoulos, "Advances in stellarator gyrokinetics" 2015 Nucl. Fusion **55** 053030
67. E.J. Doyle, W.A. Houlberg, Y. Kamada, V. Mukhovatov, T.H. Osborne, A. Polevoi, G. Bateman, J.W. Connor, J.G. Cordey, T. Fujita, X. Garbet, T.S. Hahm, L.D. Horton, A.E. Hubbard, F. Imbeaux, F. Jenko, J.E. Kinsey, Y. Kishimoto, J. Li, T.C. Luce, Y. Martin, M. Ossipenko, V. Parail, A. Peeters, T.L. Rhodes, J.E. Rice, C.M. Roach, V. Rozhansky, F. Ryter, G. Saibene, R. Sartori, A.C.C. Sips, J.A. Snipes, M. Sugihara, E.J. Synakowski, H. Takenaga, T. Takizuka, K. Thomsen, M.R. Wade, H.R. Wilson, ITPA Transport Physics Topical Group, ITPA Confinement Database and Modelling Topical Group and ITPA Pedestal and Edge Topical Group, "ITER physics basis: Chapter 2: Plasma Confinement and transport" 2007 Nucl. Fusion **47** S18
68. J Baldzuhn, H Damm, C D Beidler, K McCarthy, N Panadero, C Biedermann, S A Bozhnikov, K J Brunner, G Fuchert, Y Kazakov, M Beurskens, M Dibon, J Geiger, O Grulke, U Höfel, T Klinger, F Köchl, J Knauer, G Kocsis, P Kornejew, P T Lang, A Langenberg, H Laqua, N A Pablant, E Pasch, T S Pedersen, B Ploekel, K Rahbarnia, G Schlisio, E R Scott, T Stange, A von Stechow, T Szepesi, Y Turkin, F Wagner, V Winters, G Wurden, D Zhang and Wendelstein 7-X Team, "Pellet fueling experiments in Wendelstein 7-X" 2019 Plasma Phys. Control. Fusion **61** 095012
69. S.A. Bozhnikov, Y. Kazakov, O.P. Ford, M.N.A. Beurskens, J. Alcusón, J.A. Alonso, J. Baldzuhn, C. Brandt, K.J. Brunner, H. Damm, G. Fuchert, J. Geiger, O. Grulke, M. Hirsch, U. Höfel, Z. Huang, J. Knauer, M. Krychowiak, A. Langenberg, H.P. Laqua, S. Lazerson, N. B. Marushchenko, D. Moseev, M. Otte, N. Pablant, E. Pasch, A. Pavone, J.H.E. Proll, K. Rahbarnia, E.R. Scott, H.M. Smith, T. Stange, A. von Stechow, H. Thomsen, Yu. Turkin, G. Wurden, P. Xanthopoulos, D. Zhang, R.C. Wolf and the W7-X team, "High-performance plasmas after pellet injections in Wendelstein 7-X" 2020 Nucl. Fusion **60** 066011
70. J Baldzuhn, H Damm, C D Beidler, K McCarthy, N Panadero, C Biedermann, S A Bozhnikov, A Dinklage, K J Brunner, G Fuchert, Y Kazakov, M Beurskens, M Dibon, J Geiger, O Grulke, U Höfel, T Klinger, F Köchl, J Knauer, G Kocsis, P Kornejew, P T Lang, A Langenberg, H Laqua, N A Pablant, E Pasch, T S Pedersen, B Ploekel, K Rahbarnia, G Schlisio, E R Scott, T Stange, A Von Stechow, T Szepesi, Y Turkin, F Wagner, V Winters, G Wurden, D. Zhang and Wendelstein 7-X Team, "Enhanced energy confinement after series of pellets in Wendelstein 7-X" Plasma Phys. Control. Fusion **2020** **62** 05512
71. P. Xanthopoulos, S. A. Bozhnikov, M. N. Beurskens, H. M. Smith, G. G. Plunk, P. Helander, C. D. Beidler, J. A. Alcusón, A. Alonso, A. Dinklage, O. Ford, G. Fuchert, J. Geiger, J. H. E. Proll, M. J. Pueschel, Y. Turkin, F. Warmer, and the W7-X Team, "Turbulence Mechanisms of Enhanced Performance Stellarator Plasmas" Phys. Rev. Lett. **2020** **125** 075001

This is the author's peer reviewed, accepted manuscript. However, the online version of record will be different from this version once it has been copyedited and typeset.

PLEASE CITE THIS ARTICLE AS DOI: 10.1063/5.0047274

72. M. Romanelli, C.R. Frascati, C. Bourdelle, W. Dorland, "Effects of high density peaking and high collisionality on the stabilization of the electrostatic turbulence in the Frascati Tokamak Upgrade" 2004 Phys. Plasmas **11** 3845
73. S. P. Hirshman, K. C. Shaing, W. I. van Rij, C. O. Beasley Jr., and E. C. Crume Jr. "Plasma transport coefficients for nonsymmetric toroidal confinement systems" 1986 Phys. Fluids. **29** 2951
74. D.E. Hastings, W.A. Houlberg and K.C. Shaing, "The ambipolar electric field in stellarators" 1985 Nucl. Fusion **25** 445
75. M. Landreman, H. M. Smith, A. Mollén, and P. Helander "Comparison of particle trajectories and collision operators for collisional transport in nonaxisymmetric plasmas" 2014 Phys. Plasmas **21** 042503
76. M. Shoji, G. Kawamura, R. Smirnov, Y. Tanaka, S. Masuzaki, Y. Uesugi, N. Ashikawa, E. Gilson, R. Lunsford "Full torus impurity transport simulation for optimizing plasma discharge operation using a multi-species impurity powder dropper in the large helical device" 2019 Contrib. Plasma. Phys. **60** 5-6 Article e201900101
<https://doi.org/10.1002/ctpp.201900101>
77. F. Effenberg, A. Bortolon, H. Frerichs, B. Grierson, J. D. Lore, T. Abrams, T. E. Evans, Y. Feng, R. Lunsford, R. Maingi, A. Nagy, R. Nazikian, D. Orlov, J. Ren, D. L. Rudakov, W. R. Wampler, H. Q. Wang, "3D modeling of boron transport in DIII-D L-mode wall conditioning experiments" 2021 Nucl. Mater. Energy **26** 100900
<https://doi.org/10.1016/j.nme.2021.100900>

This is the author's peer reviewed, accepted manuscript. However, the online version of record will be different from this version once it has been copyedited and typeset.

PLEASE CITE THIS ARTICLE AS DOI: 10.1063/5.0047274

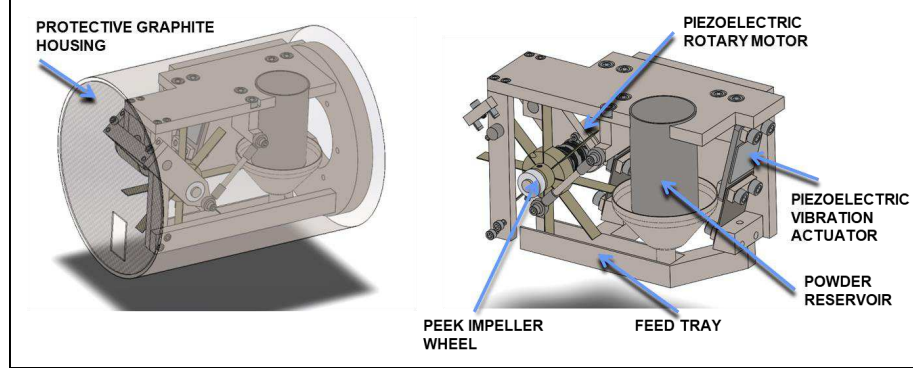
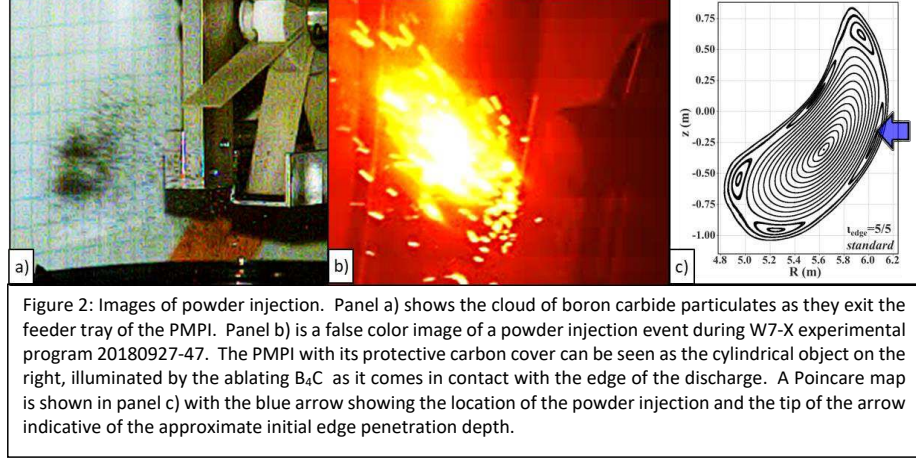


Figure 1. Assembly drawing view of PPPL Probe Mounted Particle Injector. The right hand image points out the primary components of the injector. Powder is fed from the reservoir down into the feed tray. The tray is oscillated at resonance by the piezoelectric vibration actuator which conveys the material from the rear to the front of the PMPI. Once there the powder is driven into the discharge by a rotating impeller wheel being driven at 0.35 Hz by the piezoelectric rotary motor such that the injection frequency is 2.8 Hz. The left image shows the protective graphite housing which isolates the interior workings from the surrounding discharge except for a small rectangular opening found at roughly the 6 o'clock position on the front face which allows powder injection.

This is the author's peer reviewed, accepted manuscript. However, the online version of record will be different from this version once it has been copyedited and typeset.

PLEASE CITE THIS ARTICLE AS DOI: 10.1063/5.0047274



This is the author's peer reviewed, accepted manuscript. However, the online version of record will be different from this version once it has been copyedited and typeset.

PLEASE CITE THIS ARTICLE AS DOI: 10.1063/5.0047274

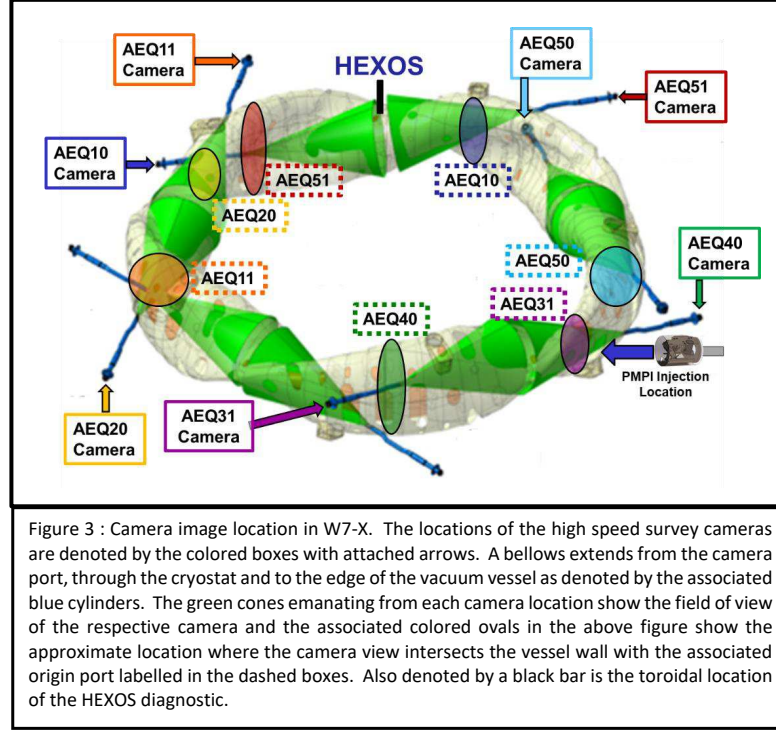


Figure 3 : Camera image location in W7-X. The locations of the high speed survey cameras are denoted by the colored boxes with attached arrows. A bellows extends from the camera port, through the cryostat and to the edge of the vacuum vessel as denoted by the associated blue cylinders. The green cones emanating from each camera location show the field of view of the respective camera and the associated colored ovals in the above figure show the approximate location where the camera view intersects the vessel wall with the associated origin port labelled in the dashed boxes. Also denoted by a black bar is the toroidal location of the HEXOS diagnostic.

This is the author's peer reviewed, accepted manuscript. However, the online version of record will be different from this version once it has been copyedited and typeset.

PLEASE CITE THIS ARTICLE AS DOI: 10.1063/5.0047274

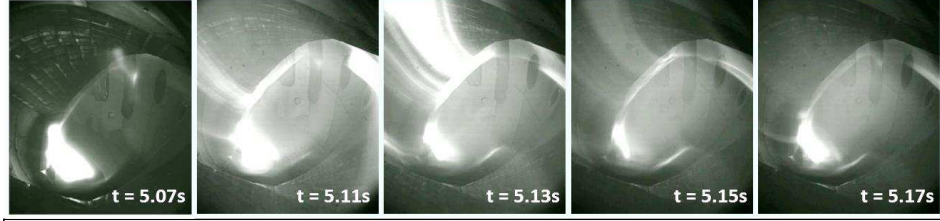


Figure 4: Evolution of field aligned impurity structures far from the injection site. Views from the visible survey camera AEQ20, approximately toroidally opposite the injection location, show the development of illuminated bands resulting from material ablation. Material is injected at $t = 5.07\text{s}$ during W7-X experimental program 20180927-47 and propagation is evidenced by the illuminated structures in the middle three panels. Given the spectral response of the visible camera, the enhanced radiation in the final panel is most likely due to radiative boron distributed poloidally throughout the plasma edge

This is the author's peer reviewed, accepted manuscript. However, the online version of record will be different from this version once it has been copyedited and typeset.

PLEASE CITE THIS ARTICLE AS DOI: 10.1063/5.0047274

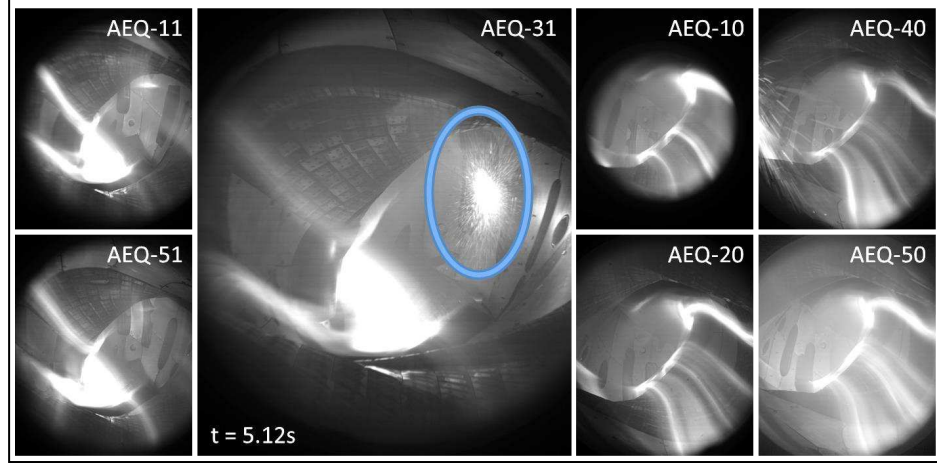
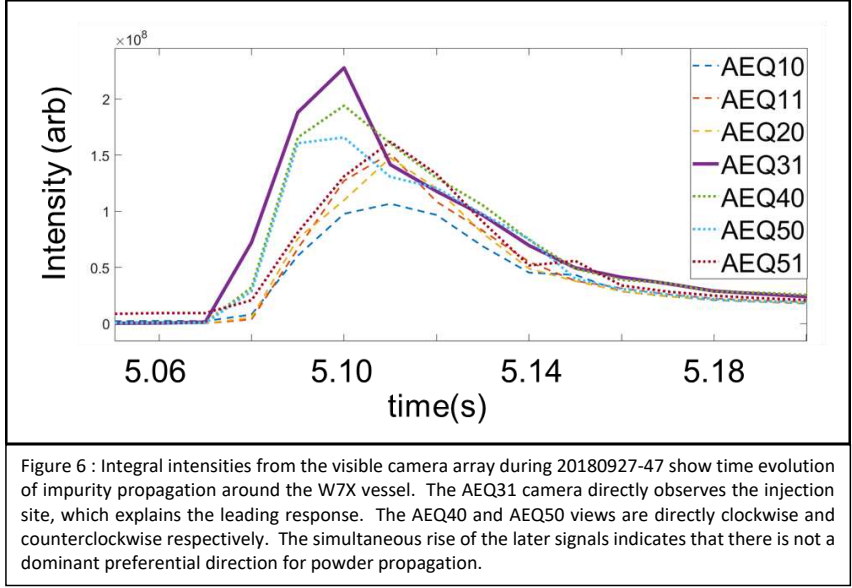


Figure 5 : The above array of images displays simultaneous views from multiple cameras providing a snapshot of impurity propagation around the internal volume during W7-X experimental program 20180927-47. The impurity pulse begins at $t = 5.07s$, and by the time of the images at $t = 5.12s$ has generated illuminated field aligned structures throughout the vessel as well as an increase in overall discharge radiation. Odd numbered panels show counter clockwise propagating views within the vessel and even numbered panels show clockwise propagating views and are inverted. The blue circle highlights the PMPI injection location in the large AEQ-31 view.

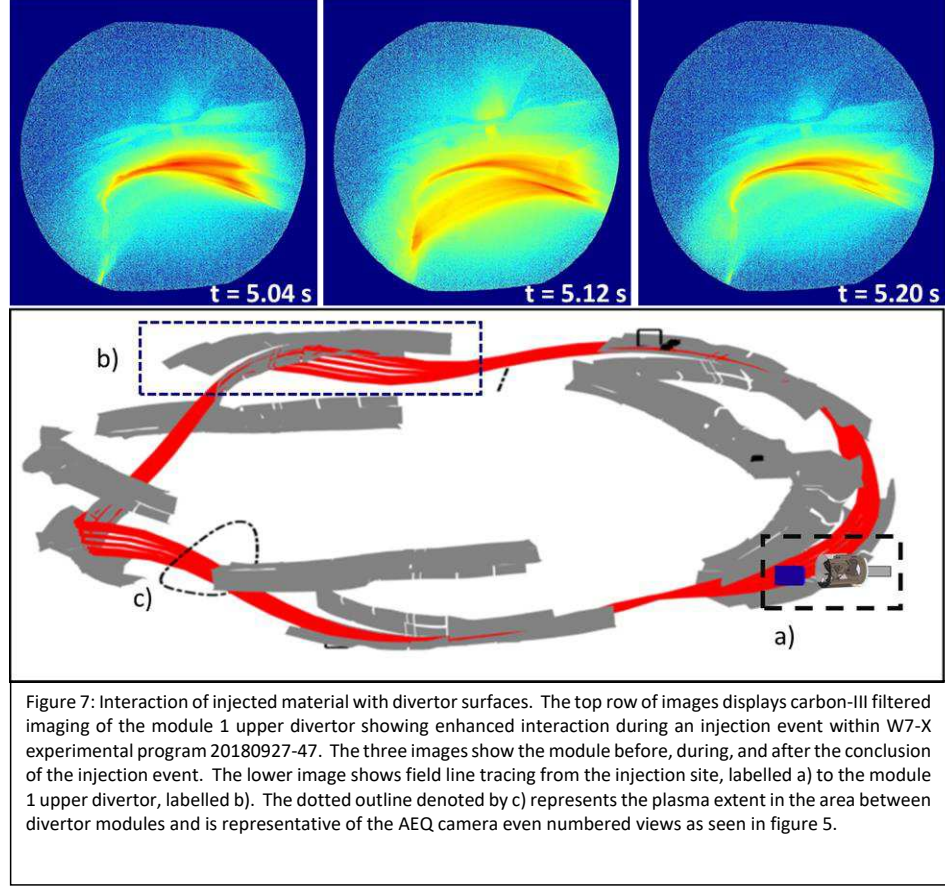
This is the author's peer reviewed, accepted manuscript. However, the online version of record will be different from this version once it has been copyedited and typeset.

PLEASE CITE THIS ARTICLE AS DOI: 10.1063/5.0047274



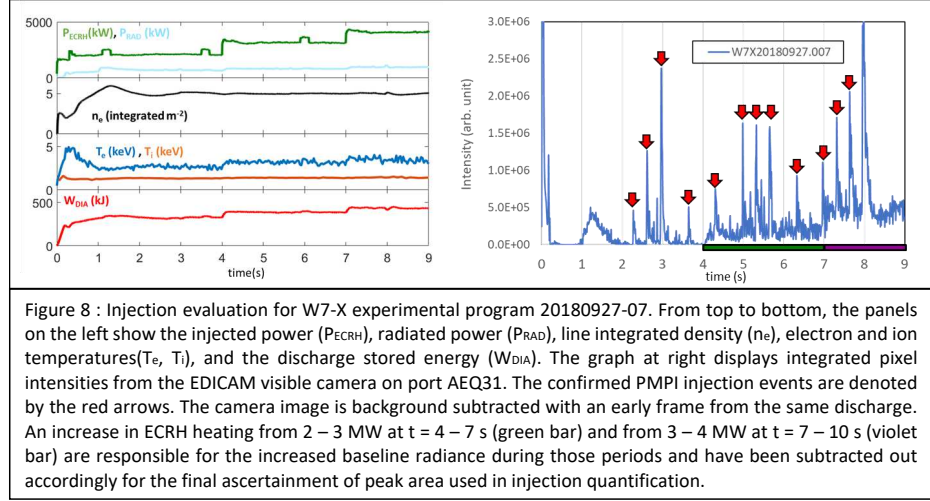
This is the author's peer reviewed, accepted manuscript. However, the online version of record will be different from this version once it has been copyedited and typeset.

PLEASE CITE THIS ARTICLE AS DOI: 10.1063/5.0047274



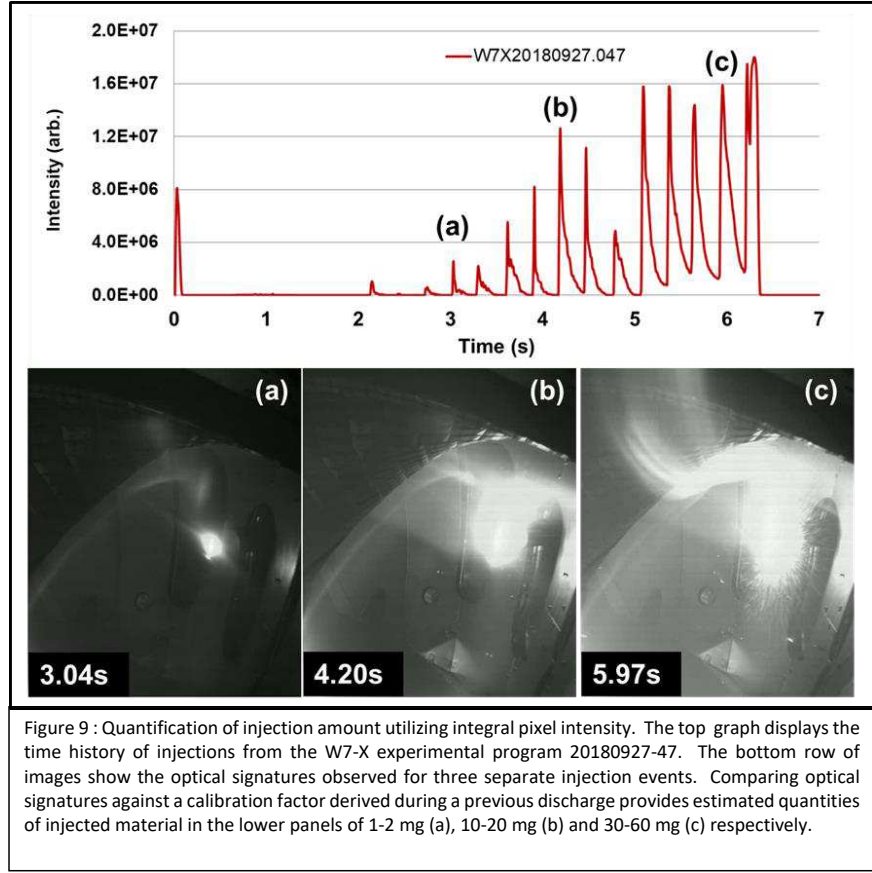
This is the author's peer reviewed, accepted manuscript. However, the online version of record will be different from this version once it has been copyedited and typeset.

PLEASE CITE THIS ARTICLE AS DOI: 10.1063/5.0047274



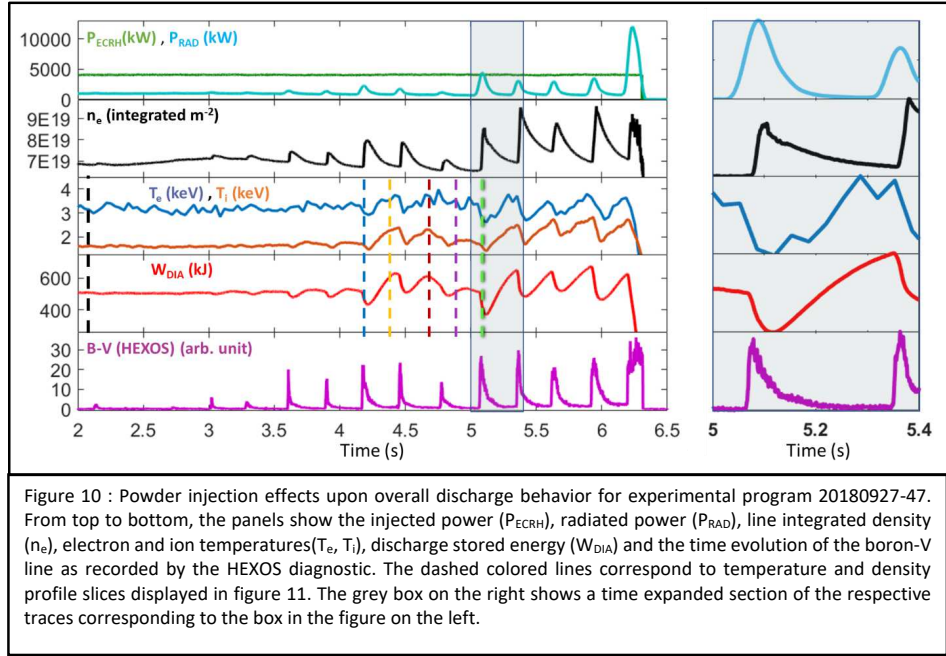
This is the author's peer reviewed, accepted manuscript. However, the online version of record will be different from this version once it has been copyedited and typeset.

PLEASE CITE THIS ARTICLE AS DOI: 10.1063/5.0047274



This is the author's peer reviewed, accepted manuscript. However, the online version of record will be different from this version once it has been copyedited and typeset.

PLEASE CITE THIS ARTICLE AS DOI: 10.1063/5.0047274



This is the author's peer reviewed, accepted manuscript. However, the online version of record will be different from this version once it has been copyedited and typeset.

PLEASE CITE THIS ARTICLE AS DOI: 10.1063/5.0047274

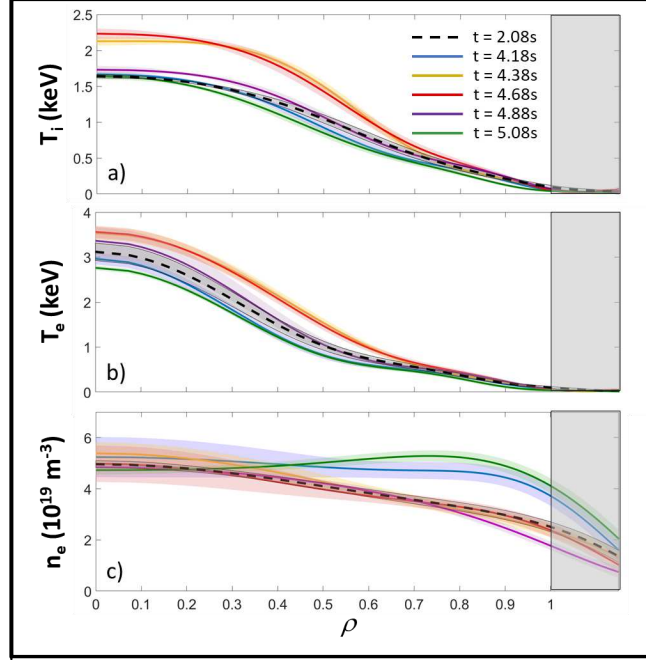
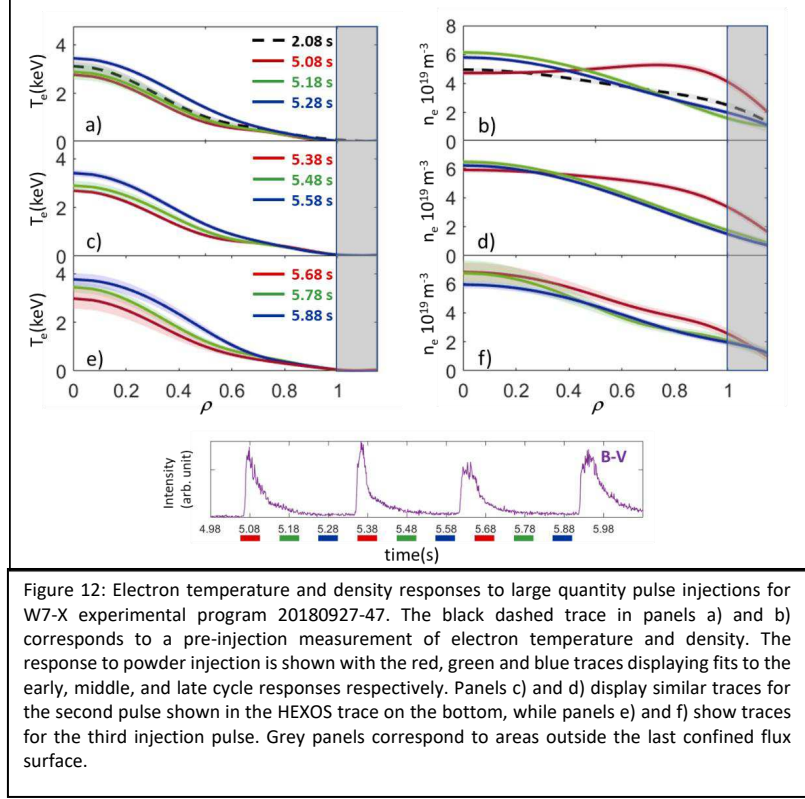


Figure 11: Evolutions in plasma profiles for ion temperature(a), electron temperature(b) and electron density(c) as a result of boron carbide pulses between 4s and 5.1s during W7-X experimental program 20180927-47. Line colors in the above graphs correspond to colored bars in Figure 10. Lines are fits to data from Thomson scattering(n_e and T_e) and x-ray imaging spectroscopy(XICS) (T_i) with error bands reflecting the scatter of the data. The grey area denotes radial locations outside the LCFS.

This is the author's peer reviewed, accepted manuscript. However, the online version of record will be different from this version once it has been copyedited and typeset.

PLEASE CITE THIS ARTICLE AS DOI: 10.1063/5.0047274



This is the author's peer reviewed, accepted manuscript. However, the online version of record will be different from this version once it has been copyedited and typeset.

PLEASE CITE THIS ARTICLE AS DOI: 10.1063/5.0047274

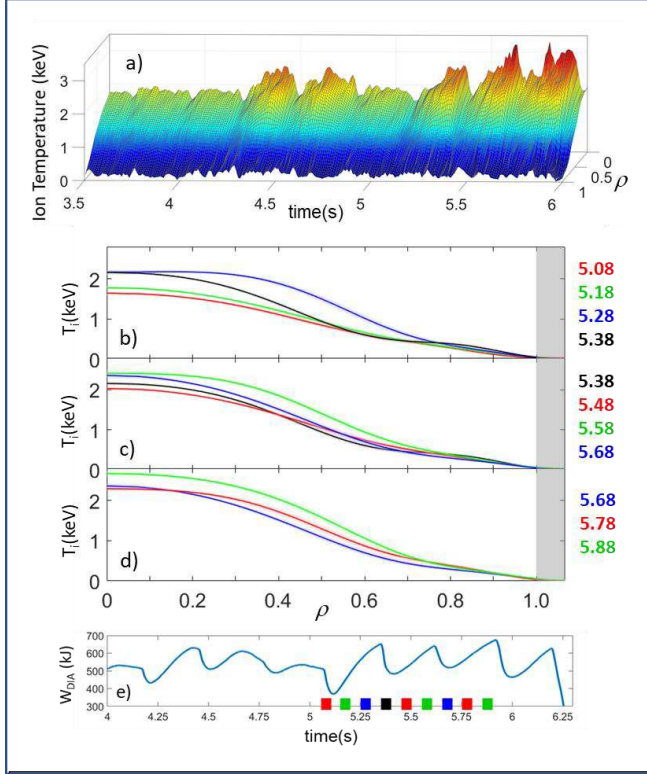


Figure 13 : Progression of ion temperature profiles in response to material injection during W7-X experimental program 20180927-47. Panel a) displays the 2D evolution of the ion temperature in response to moderate and large injections. Ion temperatures within the core above 2keV (yellow to red on the color scale) signify an elevation above those temperatures recorded in standard ECRH heated W7-X discharges. Panels b) - d) display radial profile response to PMPI injections. Note that the final time trace within panel b) is repeated in panel c) to allow evaluation of the continuing increase of core temperatures. Similarly, the final time trace within panel c) is repeated in panel d) for similar effect. The colored boxes on the x-axis of panel e) show the respective state of the plasma diamagnetic energy during the profile evaluation times.

This is the author's peer reviewed, accepted manuscript. However, the online version of record will be different from this version once it has been copyedited and typeset.

PLEASE CITE THIS ARTICLE AS DOI: 10.1063/5.0047274

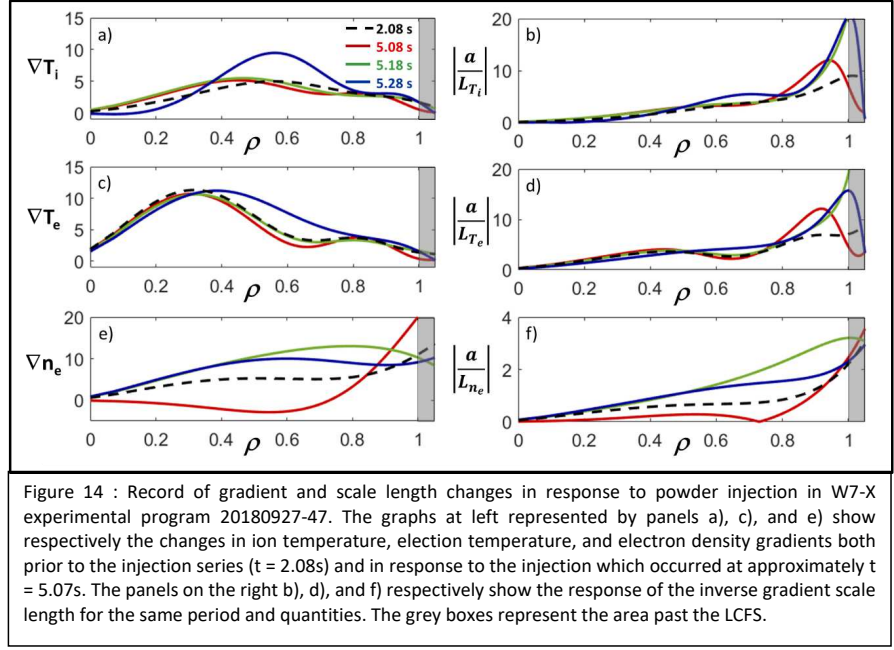


Figure 14 : Record of gradient and scale length changes in response to powder injection in W7-X experimental program 20180927-47. The graphs at left represented by panels a), c), and e) show respectively the changes in ion temperature, electron temperature, and electron density gradients both prior to the injection series ($t = 2.08$ s) and in response to the injection which occurred at approximately $t = 5.07$ s. The panels on the right b), d), and f) respectively show the response of the inverse gradient scale length for the same period and quantities. The grey boxes represent the area past the LCFS.

This is the author's peer reviewed, accepted manuscript. However, the online version of record will be different from this version once it has been copyedited and typeset.

PLEASE CITE THIS ARTICLE AS DOI: 10.1063/5.0047274

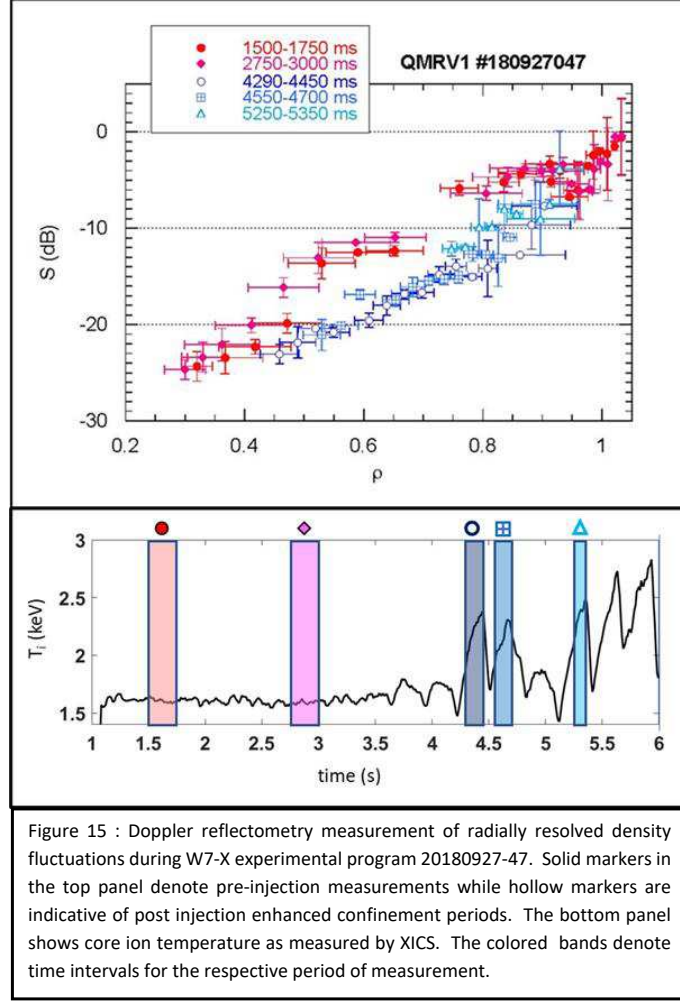
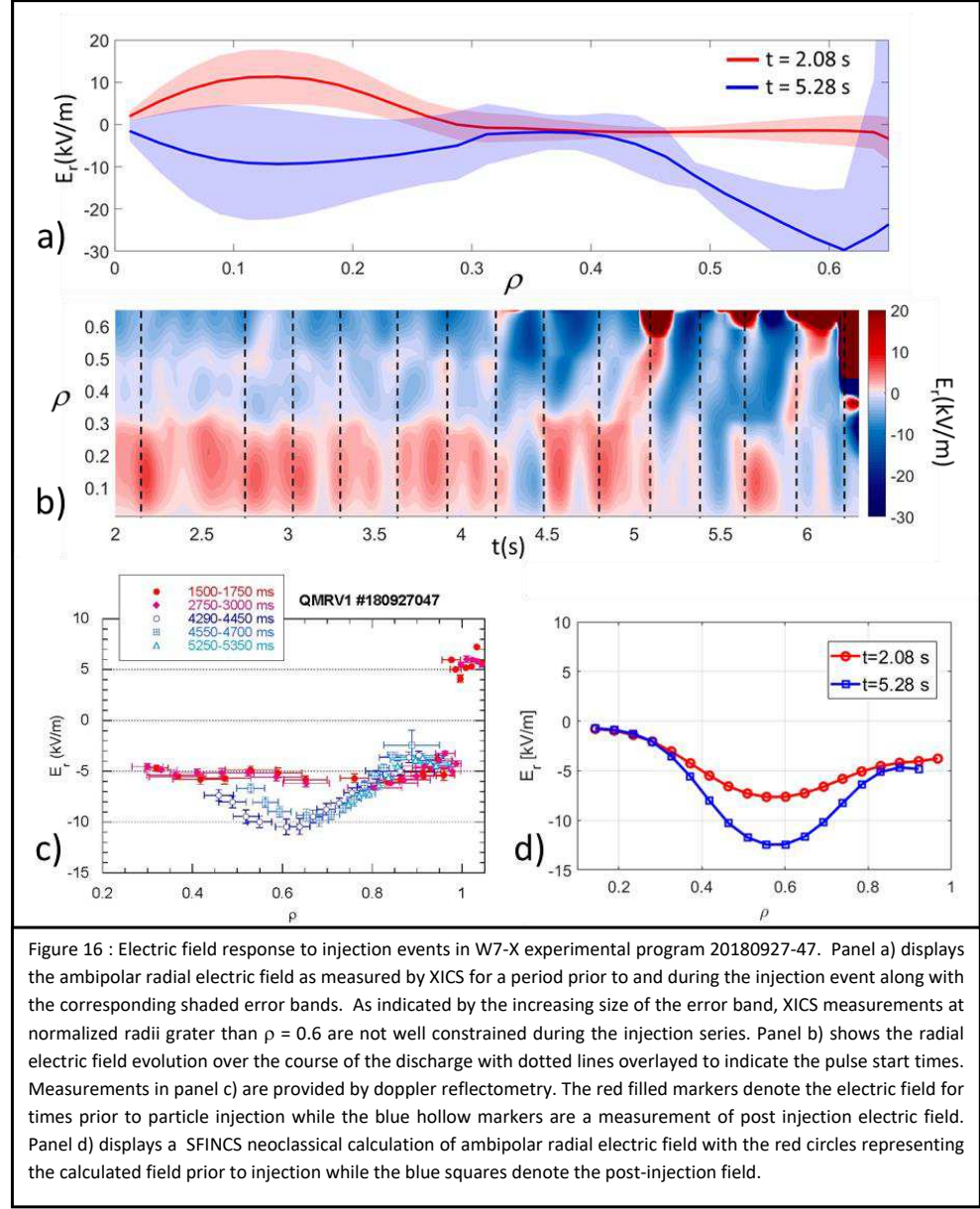


Figure 15 : Doppler reflectometry measurement of radially resolved density fluctuations during W7-X experimental program 20180927-47. Solid markers in the top panel denote pre-injection measurements while hollow markers are indicative of post injection enhanced confinement periods. The bottom panel shows core ion temperature as measured by XICS. The colored bands denote time intervals for the respective period of measurement.

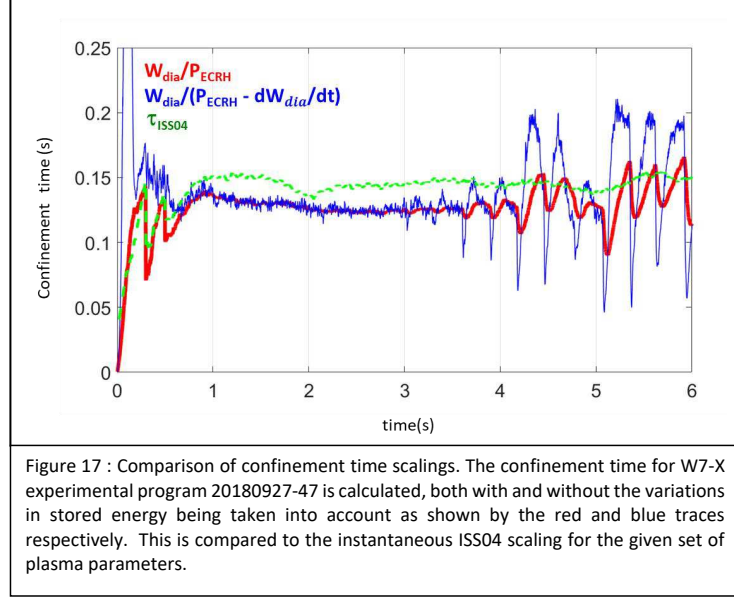
This is the author's peer reviewed, accepted manuscript. However, the online version of record will be different from this version once it has been copyedited and typeset.

PLEASE CITE THIS ARTICLE AS DOI: 10.1063/5.0047274



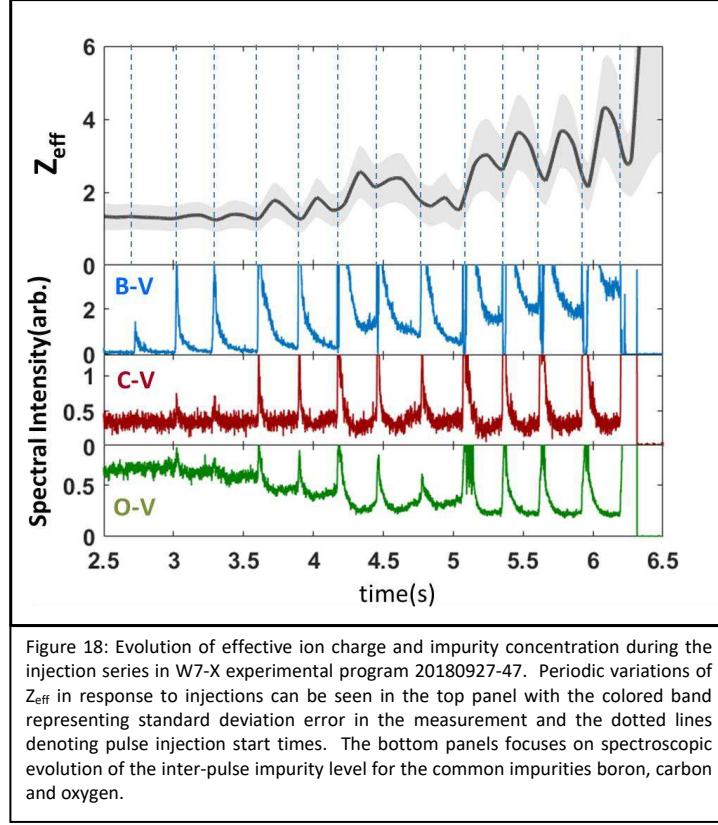
This is the author's peer reviewed, accepted manuscript. However, the online version of record will be different from this version once it has been copyedited and typeset.

PLEASE CITE THIS ARTICLE AS DOI: 10.1063/5.0047274



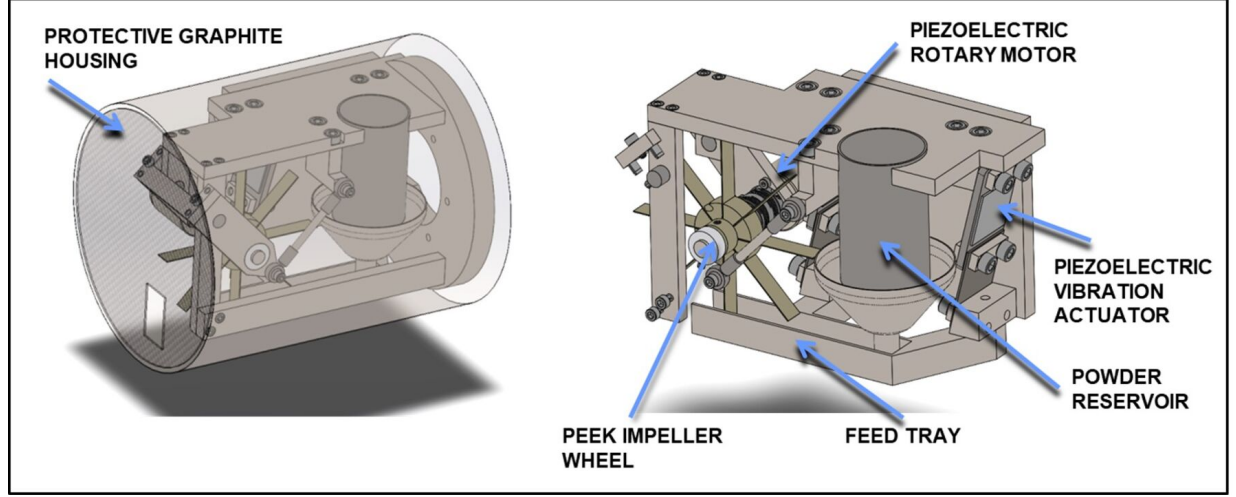
This is the author's peer reviewed, accepted manuscript. However, the online version of record will be different from this version once it has been copyedited and typeset.

PLEASE CITE THIS ARTICLE AS DOI: 10.1063/5.0047274



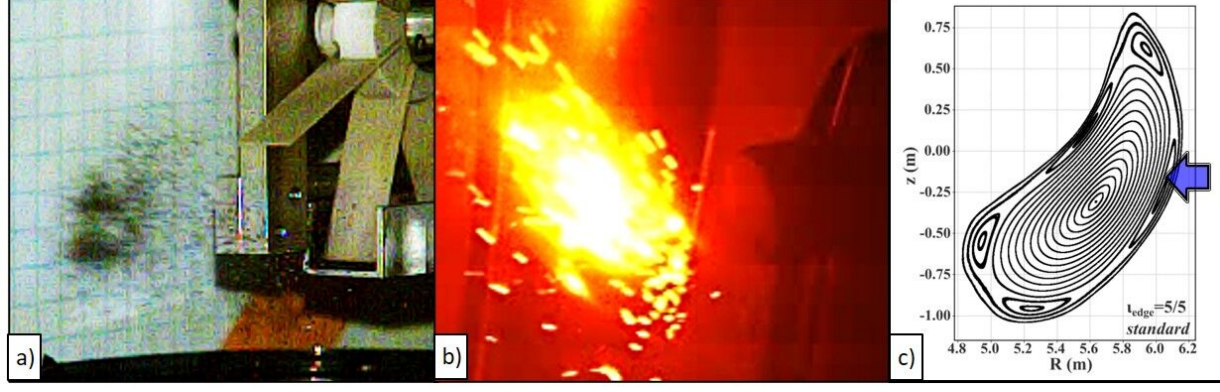
This is the author's peer reviewed, accepted manuscript. However, the online version of record will be different from this version once it has been copyedited and typeset.

PLEASE CITE THIS ARTICLE AS DOI: 10.1063/5.0047274



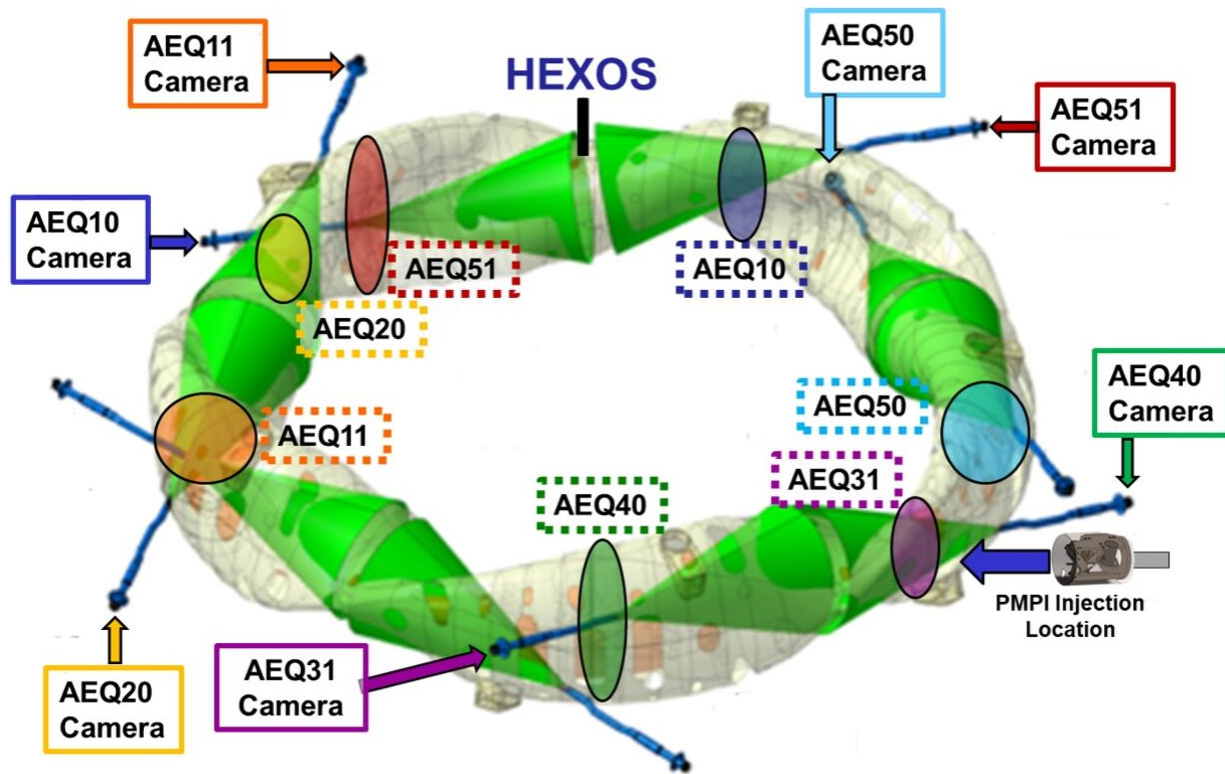
This is the author's peer reviewed, accepted manuscript. However, the online version of record will be different from this version once it has been copyedited and typeset.

PLEASE CITE THIS ARTICLE AS DOI: 10.1063/5.0047274



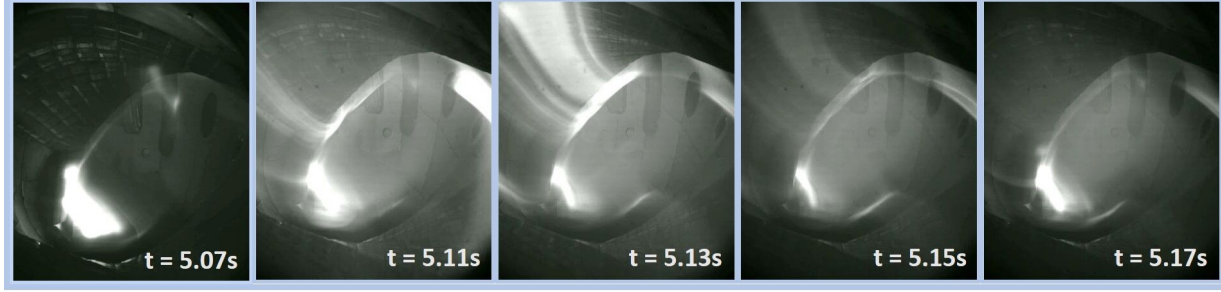
This is the author's peer reviewed, accepted manuscript. However, the online version of record will be different from this version once it has been copyedited and typeset.

PLEASE CITE THIS ARTICLE AS DOI: 10.1063/5.0047274



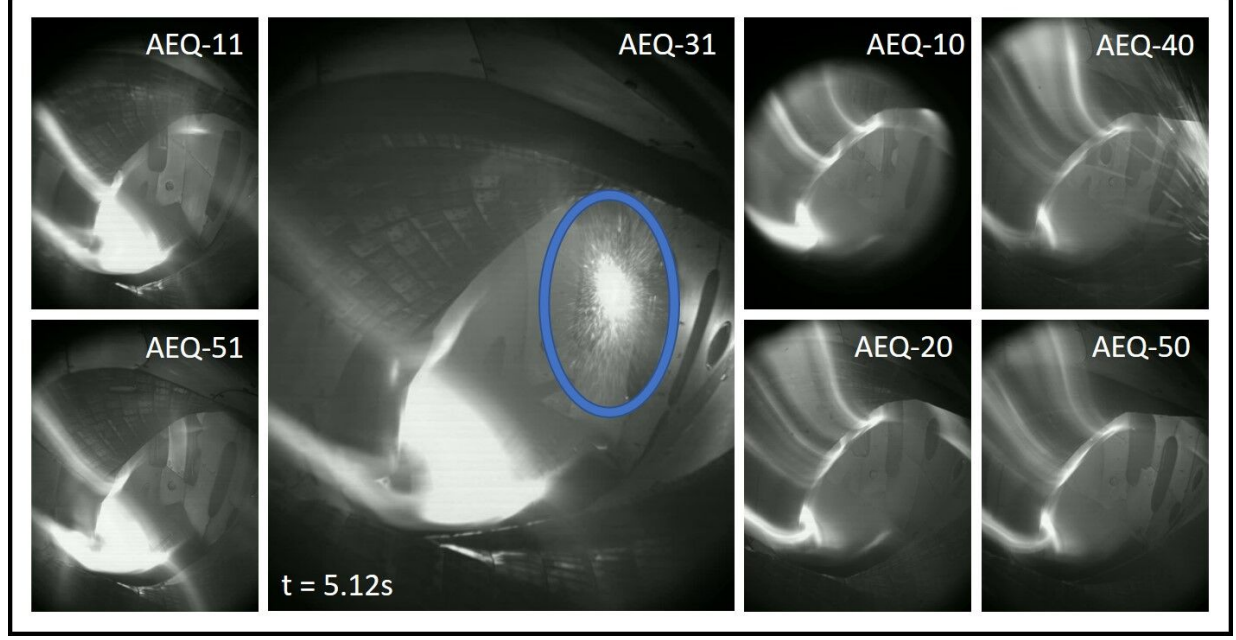
This is the author's peer reviewed, accepted manuscript. However, the online version of record will be different from this version once it has been copyedited and typeset.

PLEASE CITE THIS ARTICLE AS DOI: 10.1063/5.0047274



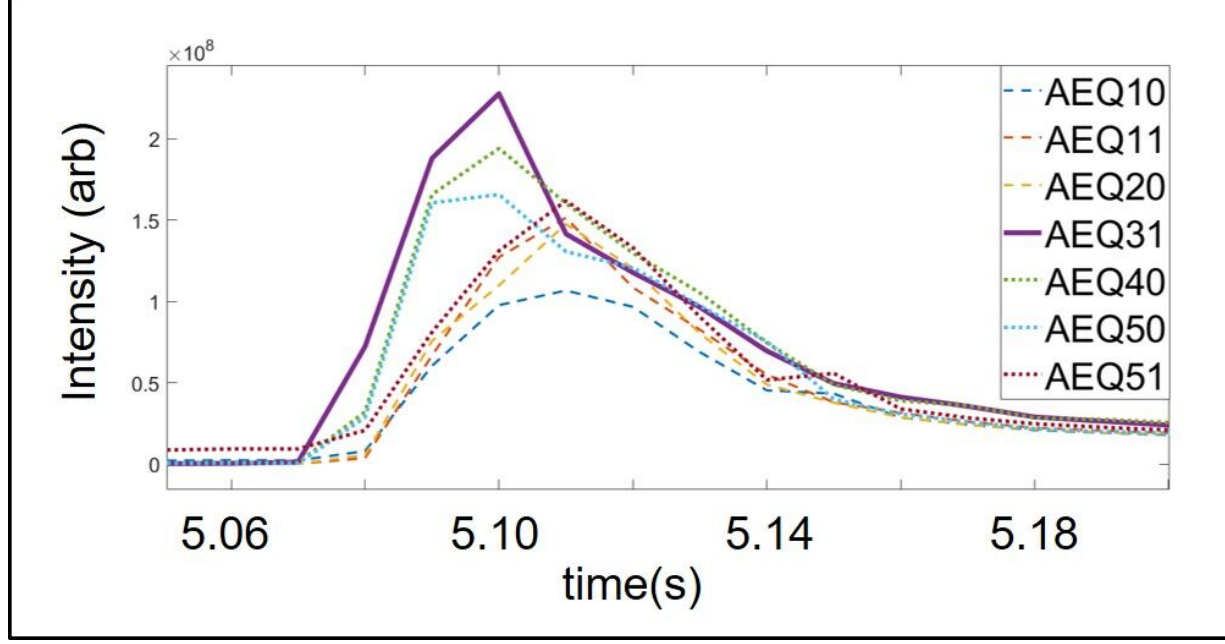
This is the author's peer reviewed, accepted manuscript. However, the online version of record will be different from this version once it has been copyedited and typeset.

PLEASE CITE THIS ARTICLE AS DOI: 10.1063/5.0047274



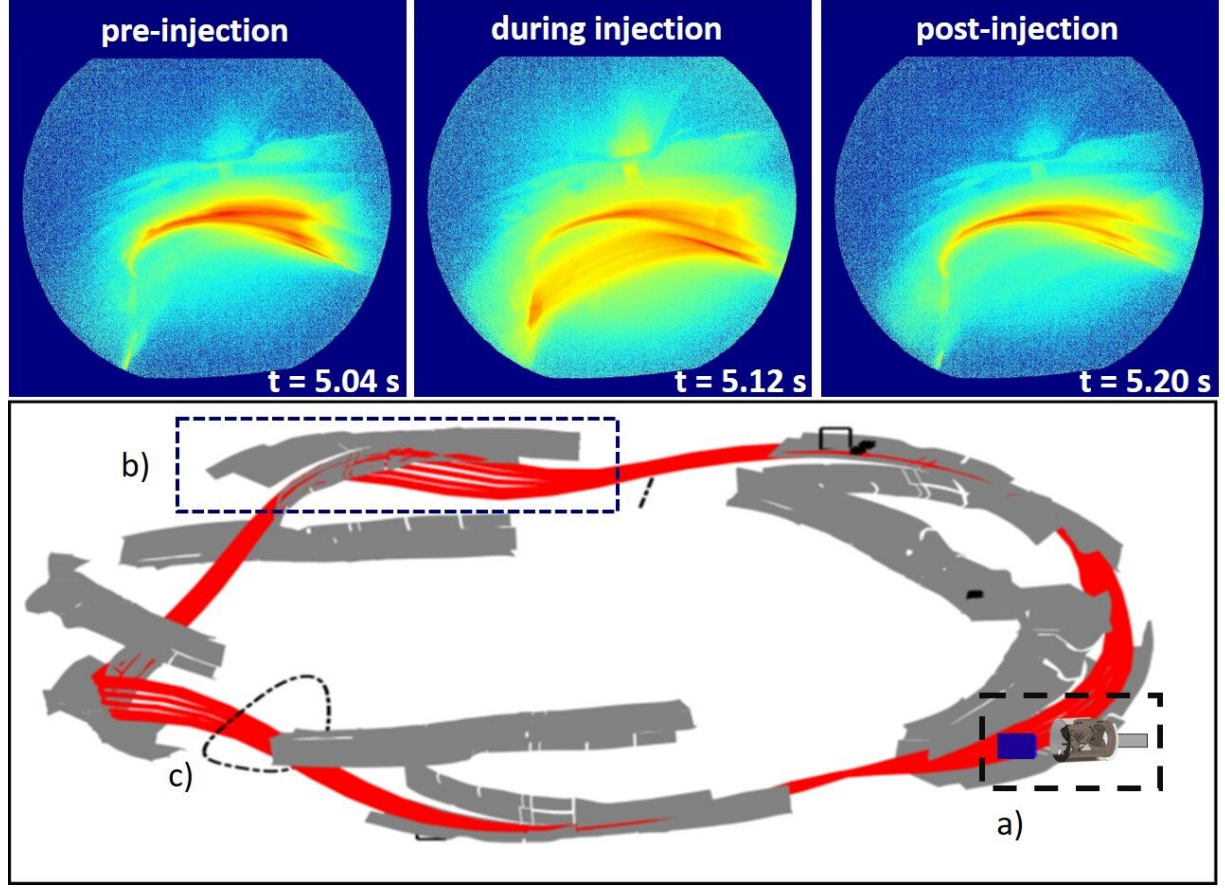
This is the author's peer reviewed, accepted manuscript. However, the online version of record will be different from this version once it has been copyedited and typeset.

PLEASE CITE THIS ARTICLE AS DOI: 10.1063/5.0047274



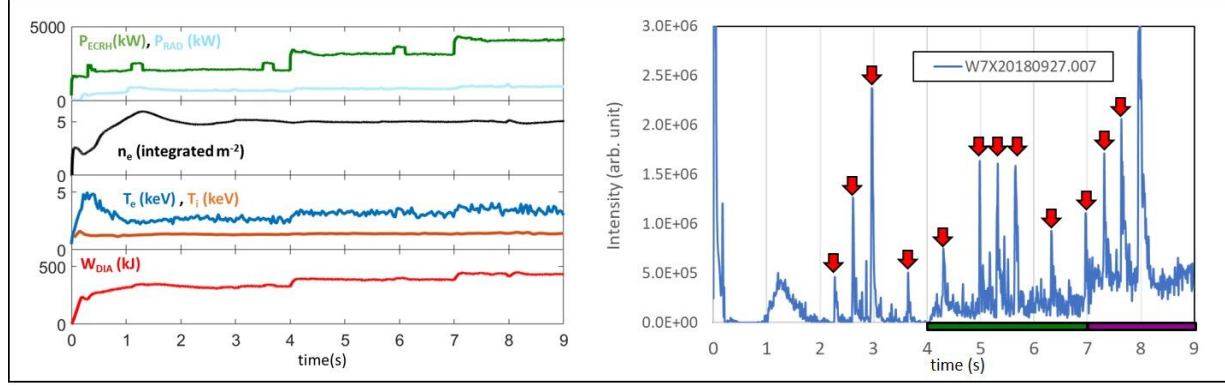
This is the author's peer reviewed, accepted manuscript. However, the online version of record will be different from this version once it has been copyedited and typeset.

PLEASE CITE THIS ARTICLE AS DOI: 10.1063/5.0047274



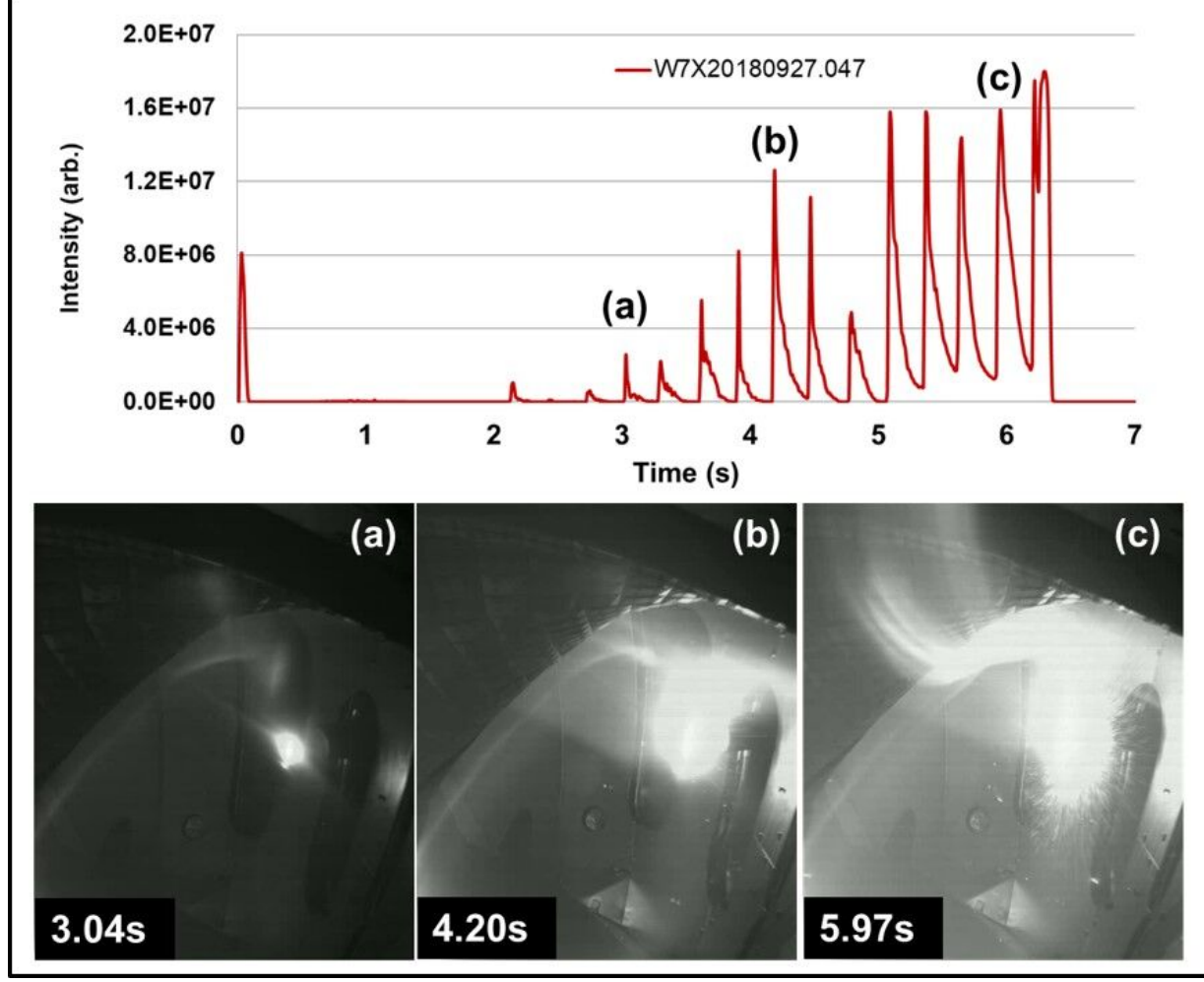
This is the author's peer reviewed, accepted manuscript. However, the online version of record will be different from this version once it has been copyedited and typeset.

PLEASE CITE THIS ARTICLE AS DOI: 10.1063/5.0047274



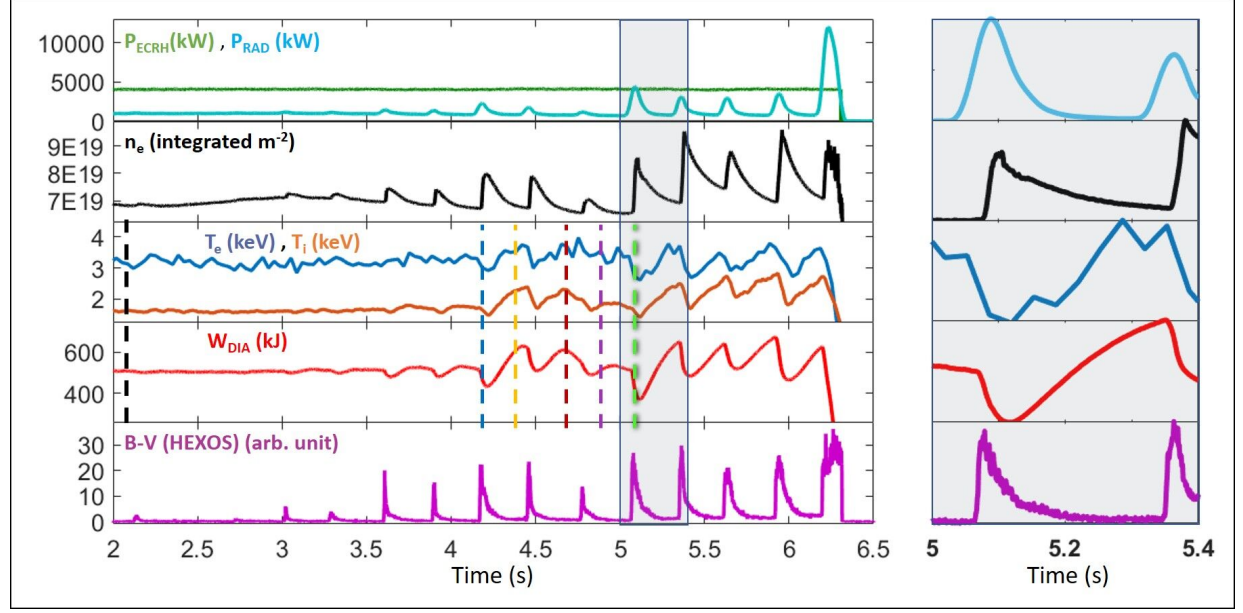
This is the author's peer reviewed, accepted manuscript. However, the online version of record will be different from this version once it has been copyedited and typeset.

PLEASE CITE THIS ARTICLE AS DOI: 10.1063/5.0047274



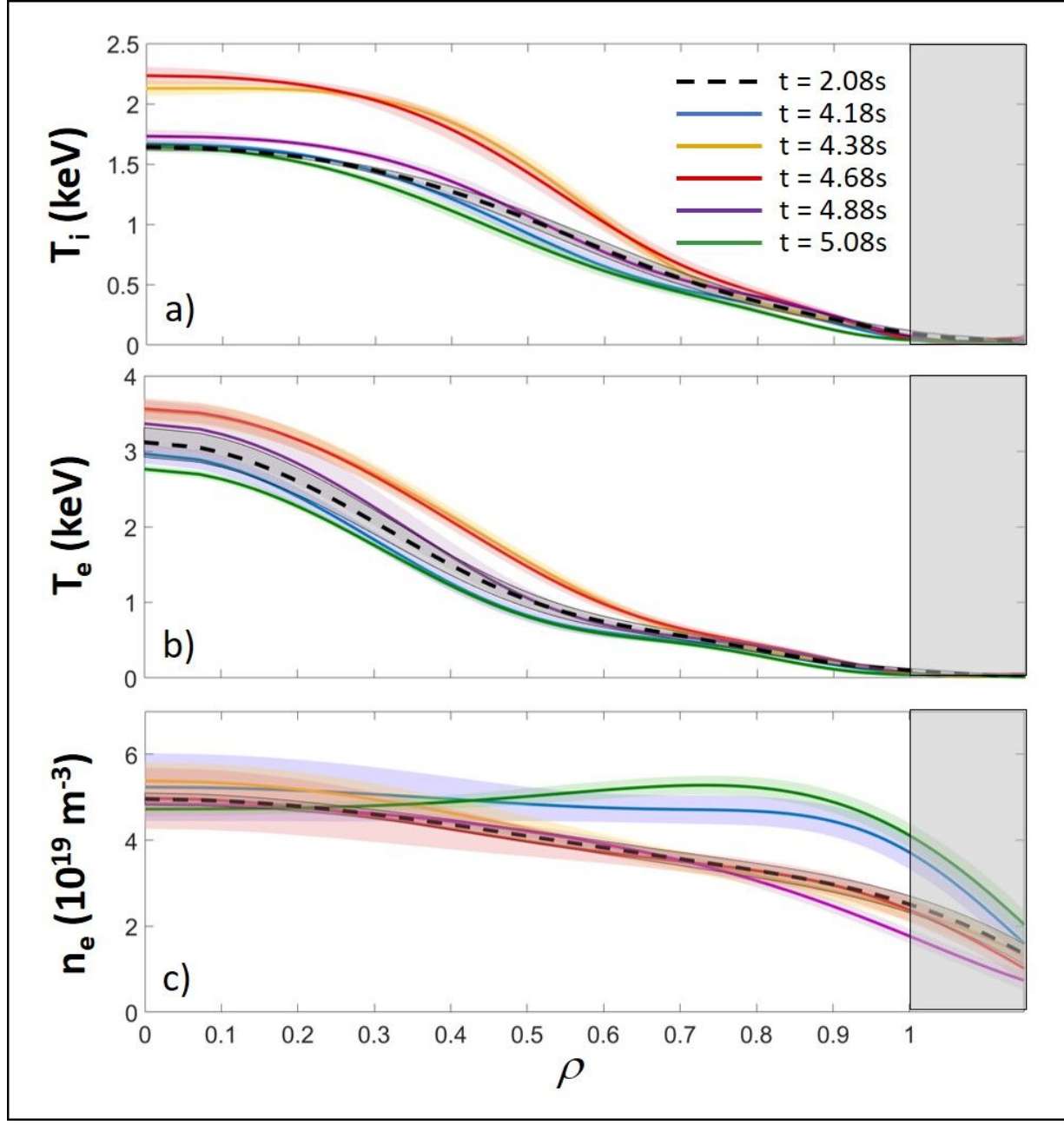
This is the author's peer reviewed, accepted manuscript. However, the online version of record will be different from this version once it has been copyedited and typeset.

PLEASE CITE THIS ARTICLE AS DOI: 10.1063/5.0047274



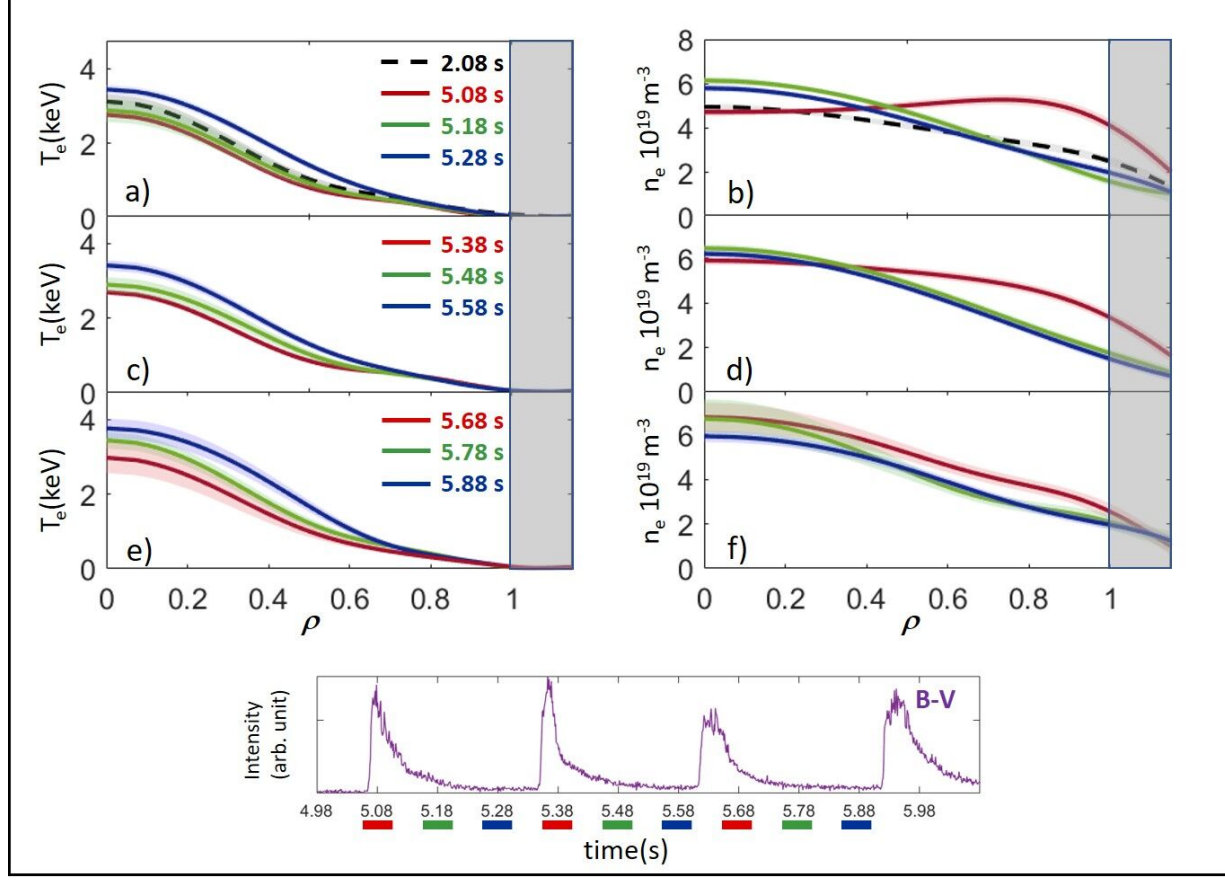
This is the author's peer reviewed, accepted manuscript. However, the online version of record will be different from this version once it has been copyedited and typeset.

PLEASE CITE THIS ARTICLE AS DOI: 10.1063/5.0047274



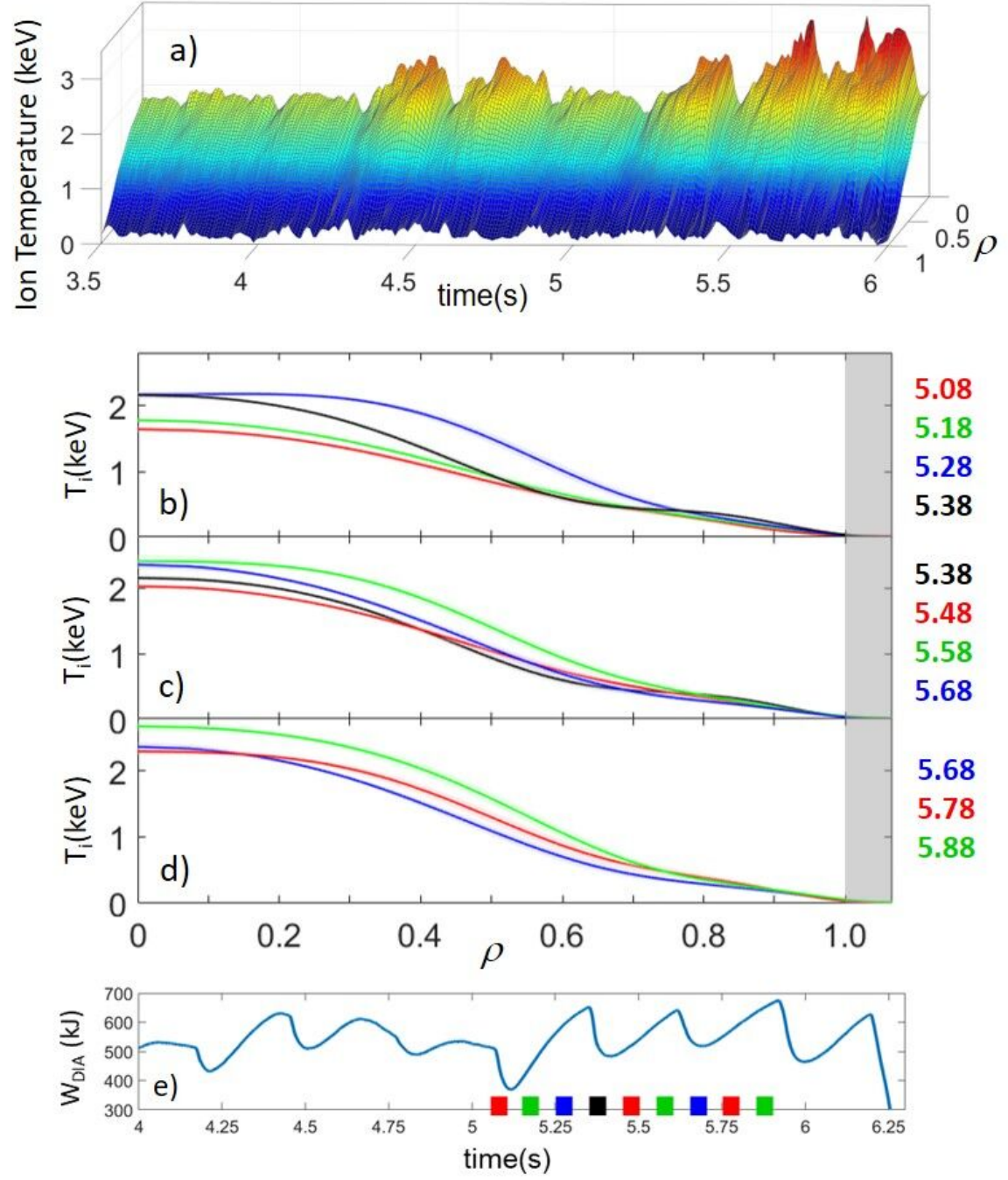
This is the author's peer reviewed, accepted manuscript. However, the online version of record will be different from this version once it has been copyedited and typeset.

PLEASE CITE THIS ARTICLE AS DOI: 10.1063/5.0047274



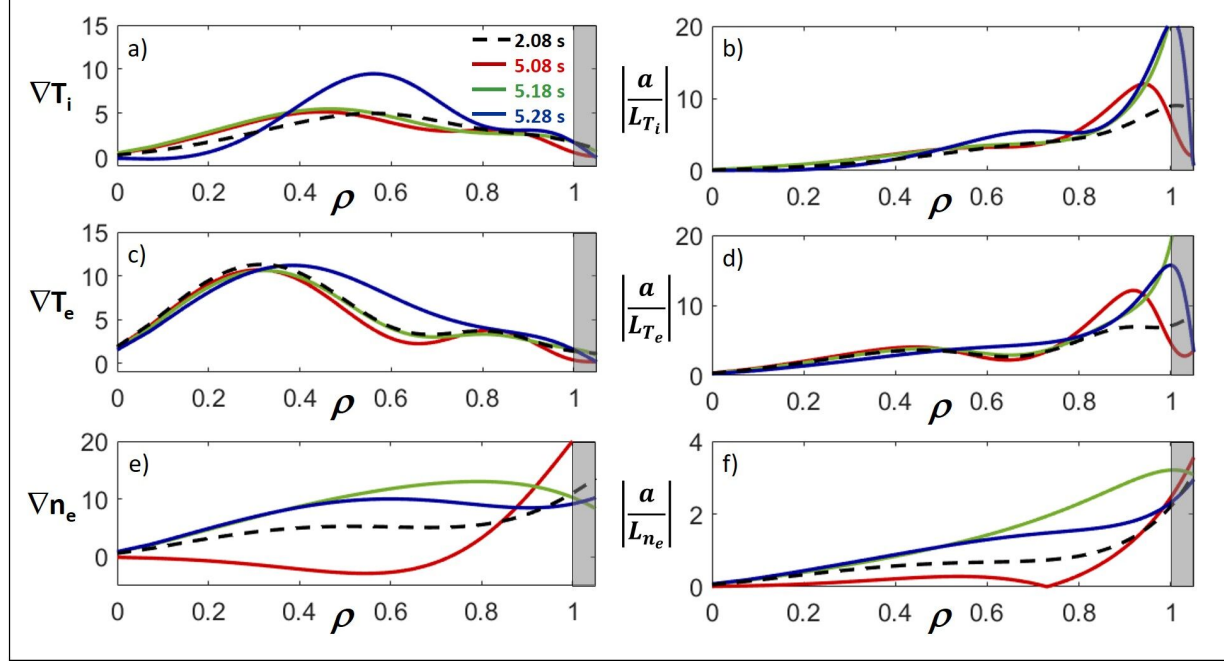
This is the author's peer reviewed, accepted manuscript. However, the online version of record will be different from this version once it has been copyedited and typeset.

PLEASE CITE THIS ARTICLE AS DOI: 10.1063/5.0047274

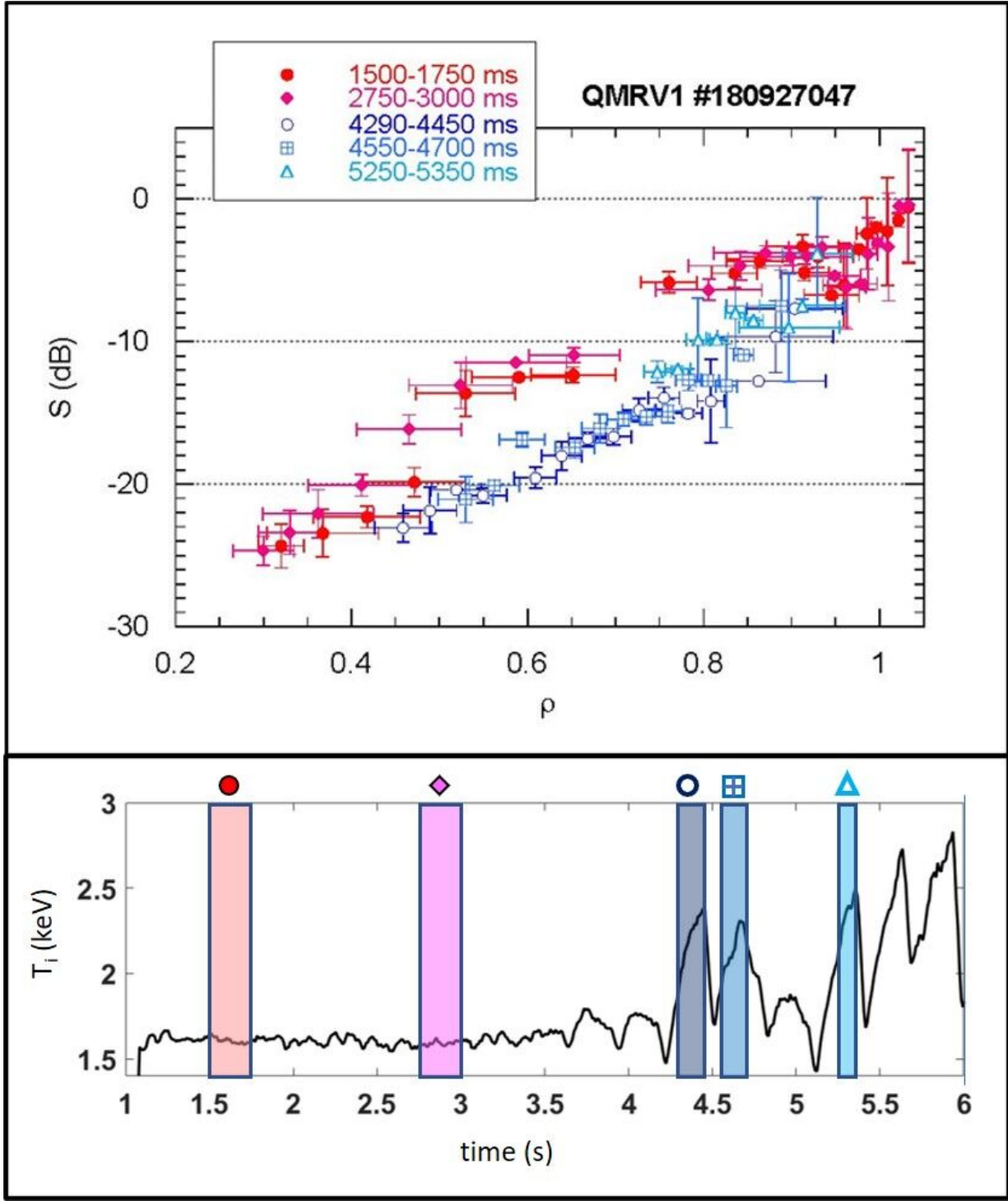


This is the author's peer reviewed, accepted manuscript. However, the online version of record will be different from this version once it has been copyedited and typeset.

PLEASE CITE THIS ARTICLE AS DOI: 10.1063/5.0047274

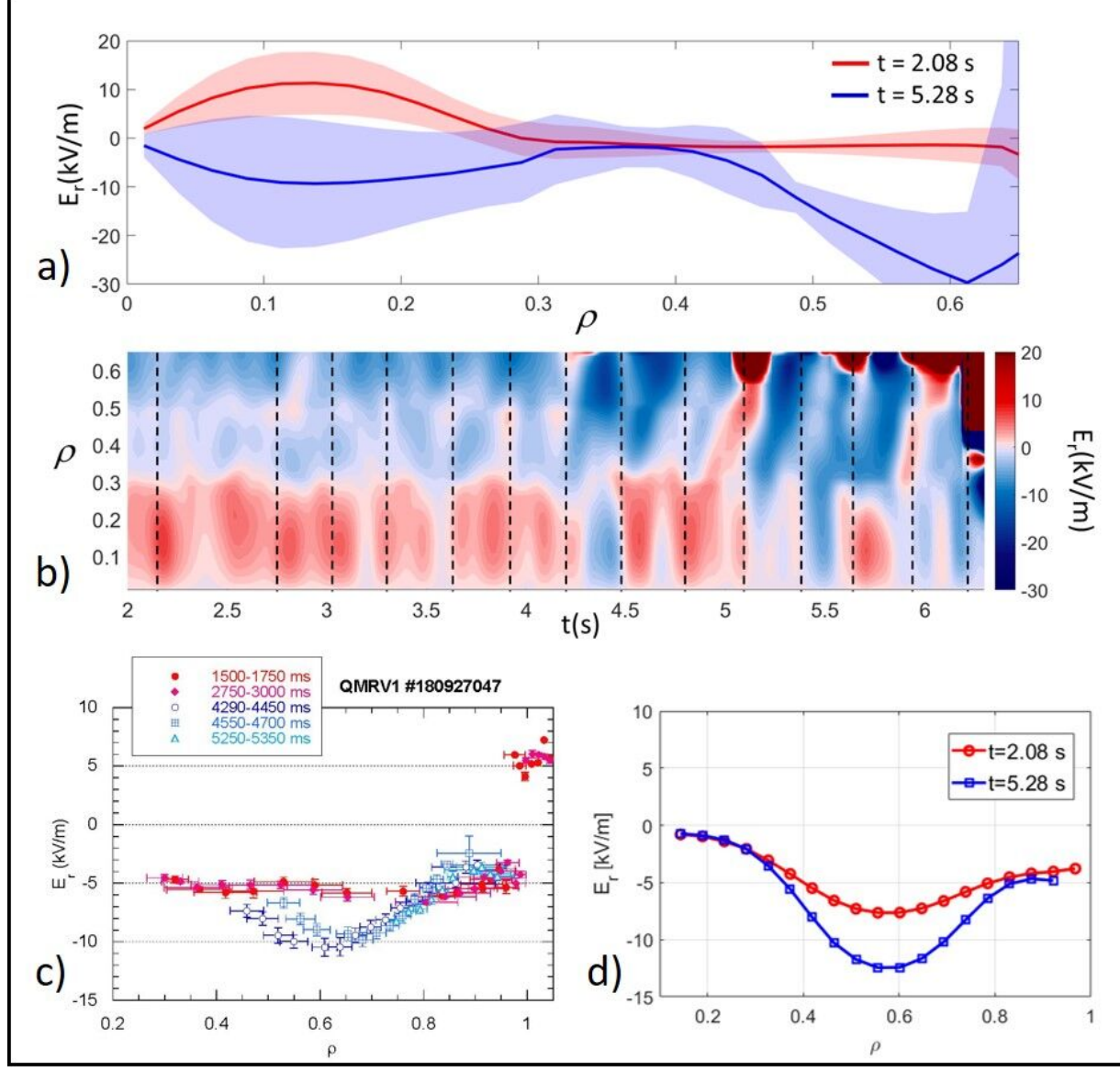


This is the author's peer reviewed, accepted manuscript. However, the online version of record will be different from this version once it has been copyedited and typeset.
PLEASE CITE THIS ARTICLE AS DOI: 10.1063/5.0047274



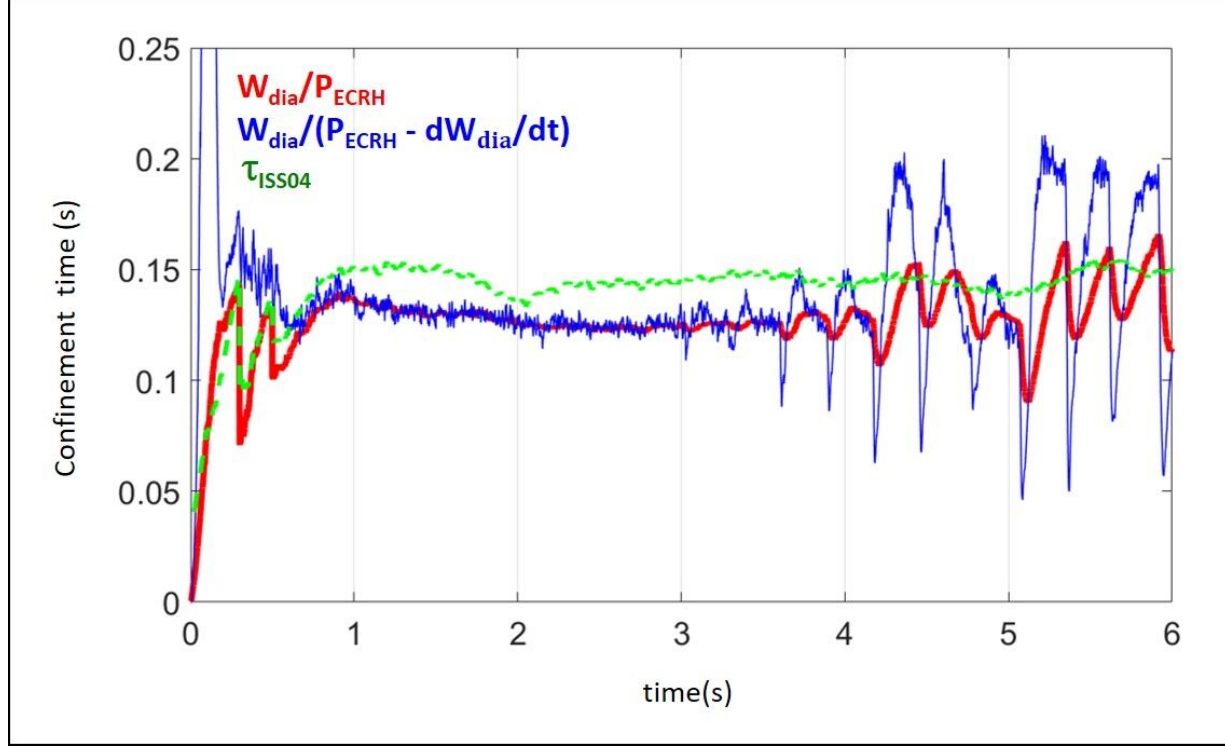
This is the author's peer reviewed, accepted manuscript. However, the online version of record will be different from this version once it has been copyedited and typeset.

PLEASE CITE THIS ARTICLE AS DOI: 10.1063/5.0047274



This is the author's peer reviewed, accepted manuscript. However, the online version of record will be different from this version once it has been copyedited and typeset.

PLEASE CITE THIS ARTICLE AS DOI: 10.1063/5.0047274



This is the author's peer reviewed, accepted manuscript. However, the online version of record will be different from this version once it has been copyedited and typeset.

PLEASE CITE THIS ARTICLE AS DOI: 10.1063/5.0047274

